Update of the NEXT ion thruster service life assessment with post-test correlation to the long duration test

IEPC-2017-061

Presented at the 35th International Electric Propulsion Conference
Georgia Institute of Technology • Atlanta, Georgia • USA
October 8 – 12, 2017

John T. Yim,[1] George C. Soulas,[2] Rohit Shastry,[3] Maria Choi,[4] Jonathan A. Mackey,[5]
and Timothy R. Sarver-Verhey[6]
NASA Glenn Research Center, Cleveland, OH, 44135, USA

The service life assessment for NASA's evolutionary xenon thruster (NEXT) is updated to incorporate the results from the successful and voluntarily early completion of the 51,184 h long duration test (LDT) which demonstrated 918 kg of total xenon throughput. The results of the numerous post-test investigations including destructive interrogations have been assessed against all of the critical known and suspected failure mechanisms to update the life and throughput expectations for each major component. Analysis results of two of the most acute failure mechanisms—namely pit-and-groove erosion and aperture enlargement of the accelerator grid—are not updated in this work, but will be published at a future time after analysis completion.

I. Introduction

NASA's evolutionary xenon thruster (NEXT) offers the potential to enable and enhance numerous mission concepts through its demonstrated high specific impulse and efficiency capabilities. These missions will also require high reliability and lifetime capabilities as well. Previous work provided a thruster service life assessment based on known failure modes and wear processes.[1,2] This report provides an update to the service life assessment based on new information and data obtained in the past decade since the original life assessment. Primary to this is the successful completion of the long duration test (LDT) of NEXT, where over 50 kh of operation and 900 kg of propellant were processed.[3] Results of the test, including destructive examination of the thruster components, have been underway and are being used to further validate or update various aspects of the service life assessment. The purpose of this service life assessment is to provide analysis of the various thruster failure modes with estimates of how long they may be expected to operate reliably. These results can then be used as a general guide for mission planning and requirements with respect to expected thruster operational life.

A number of life limiting mechanisms for gridded ion thrusters have been identified and assessed over the years and are listed below in Table 1.[1,4,5] Some of the failure modes listed in the references have since been eliminated via design well before the LDT and are not discussed further here. In addition, some of those other failure modes are not addressed at the thruster level, which is the focus here, but rather more directly involve other system components such as the power processing unit (PPU). For the remaining potential thruster failure mechanisms, they are addressed via three general approaches:

[1] Research aerospace technologist, Electric propulsion systems branch, john.t.yim@nasa.gov.
[2] Research aerospace technologist, Electric propulsion systems branch, george.c.soulas@nasa.gov.
[3] Research aerospace technologist, Electric propulsion systems branch, rohit.shastry@nasa.gov.
[4] Research aerospace technologist, Electric propulsion systems branch, maria.choi@nasa.gov.
[5] Research aerospace technologist, Electric propulsion systems branch, jonathan.a.mackey@nasa.gov.
[6] Research aerospace technologist, Electric propulsion systems branch, timothy.r.verhey@nasa.gov.

1) Gradual wear mechanisms

   These potential failure modes can be described and modeled in a deterministic fashion. This includes all of the mechanisms involving ion impact sputter erosion of various thruster surfaces as well as barium depletion of the cathode inserts. The approach in characterizing these modes is to use analysis and models—anchored to LDT data where appropriate—to calculate the resulting expected throughput and life capability before the wear leads to a failure. Sufficient conservatism is included in the evaluation to provide comfortable margins on the expected life.

2) Probabilistic event description failures

   These failure modes are not as readily captured by a gradual, observable wear rate. Either the wear rate is difficult to interrogate and model in a deterministic fashion, such as cathode heater cyclic failures, or are dependent on chance events occurring, such as debris or flake contamination grid shorting. These modes are better described and assessed using probabilistic techniques, such as Weibull distribution analysis, to provide failure rates that can be incorporated into a system-level probabilistic risk assessment.

3) Failure modes eliminated via design

   These failure modes are deemed non-credible through inherent design aspects of the NEXT system. For example, proper shadow shielding incorporated into the thruster design can remove the potential of the loss of electrical isolation via sputter deposition. Proper thermal design can provide generous temperature margins for the discharge chamber magnets. These modes should be examined with extreme care to ensure the failures are indeed eliminated via design for NEXT with supporting evidence from the LDT and other thruster tests.

Each of the items listed in Table 1 will be examined point-by-point to provide a comprehensive view of the service life assessment for NEXT. To note, each of the cathode wear mechanisms listed generally apply to both the discharge and neutralizer cathodes, though the specific details will of course be different. Later in this report, the 'C' designation as shown in Table 1 will apply specifically to the discharge cathode assembly (DCA), while similar 'D' designations will be used to refer to the neutralizer cathode assembly (NCA) assessment. Note that the post-LDT result correlated analysis and modeling of the first two mechanisms listed—pit and groove erosion and aperture enlargement of the accelerator grid—were not completed in time for this paper, but will be presented at a later time. It should also be noted that these two mechanisms are suspected to be the most limiting for the service life for NEXT.

Table 1: Gridded ion thruster life-limiting mechanisms

Component		Failure mechanism
Ion optics	A1	Pit and groove erosion of accelerator grid leading to structural yielding or failure
	A2	Barrel erosion and enlargement of accelerator grid apertures leading to electron backstreaming
	A3	Accelerator grid rogue hole formation leading to electron backstreaming
	A4	Screen grid erosion leading to structural yielding/failure and exposure of accelerator grid
	A5	Deposition or flake contamination leading to unclearable grid shorts
Discharge chamber	B1	Overheating and degradation of magnetic field strength
	B2	Deposition of sputtered material or other degradation reducing electrical isolation
Hollow cathodes	C1	Erosion of cathode keeper leading to exposure of cathode orifice plate and heater to wear
	C2	Erosion of cathode orifice leading to transition to plume mode or loss of orifice
	C3	Deposition leading to orifice clogging or keeper-cathode shorting
	C4	Depletion or tungstate/poisoning locking of insert barium impregnate
	C5	Degradation of heater insulation or conductor, leading to short or open circuit

The criteria for service life in this report will be generally expressed as propellant throughput with operating duration also listed as appropriate. Since the relation between throughput and duration is dependent on the operating condition—and for mission applications, the throttling profiles—there is no constant one-to-one correlation between the two. In general, though, the maximum power and flow rate throttle level condition, TL40 (1800 V, 3.52 A), will be used as a worst-case setting, and the life assessment throughput and duration will be expressed assuming this condition unless explicitly stated otherwise. For certain wear modes where other operating conditions may be more

stressing, those will be specifically called out in this report and clearly identified. Where possible, comparisons to LDT data will be presented. The general LDT throttling profile is presented below in Table 2. Additional data of measured thruster operating parameters from the LDT that will be used in the analyses reported in this document are shown in Table 3. Generally averaged data from over the course of the LDT are shown, but some exceptions (e.g. maximums, beginning of life (BOL) values, etc.) are used and marked as such.

Table 2: Long duration test throttling profile

Throttle segment	Throttle level	Operating condition	Segment duration	Total mass flow rate
1	TL40	1800 V, 3.52 A	13.0 kh	20.6 kg/kh
2	TL37	1179 V, 3.52 A	6.5 kh	20.6 kg/kh
3	TL05	679 V, 1.20 A	3.4 kh	7.3 kg/kh
4	TL01	275 V, 1.00 A	3.2 kh	6.6 kg/kh
5	TL12	1800 V, 1.20 A	3.1 kh	7.3 kg/kh
6	TL40	1800 V, 3.52 A	21.9 kh	20.6 kg/kh

Table 3: NEXT parameters measured during the LDT

Throttle level	Operating condition	Discharge cathode current	Discharge keeper current	Corrected screen grid current (BOL)	Screen grid to cathode common voltage
TL40	1800 V, 3.52 A	19.4 A (max), 19.0 A (avg)	0.214 A	405 mA	-0.983 V
TL37	1179 V, 3.52 A	20.8 A (max), 20.4 A (avg)	0.232 A	709 mA	-1.165 V
TL12	1800 V, 1.20 A	8.7 A (max), 8.5 A (avg)	0.087 A	150 mA	-0.511 V
TL05	679 V, 1.20 A	9.8 A (max), 9.3 A (avg)	0.098 A	179 mA	-0.408 V
TL01	275 V, 1.00 A	8.3 A (max), 8.1 A (avg)	0.086 A	109 mA	-0.411 V

II. Ion Optics

A1. Accelerator grid pit-and-groove erosion

The primary suspected life-limiting mechanism for NEXT is pit-and-groove erosion of the accelerator grid leading to eventual structural failure.[1] Prior analyses have estimated that the grids should handle over 750 kg of throughput before penetration over most of the throttle table except for the three lowest power settings.[1,2] Accelerator grid penetration was previously estimated to occur at minimums of 330 kg of throughput (45 kh run time) at TL01 or 36 kh of run time (750 kg throughput) at TL40.[2] While the LDT successfully demonstrated over 50 kh of operation and over 900 kg of throughput without any grid failure, post-test evaluation of the grids displayed an unanticipated net carbon deposition within the pit-and-groove pattern.[6] The net erosion process within the pits-and-grooves appears to transition to a net carbon deposition process after approximately 36.5 kh. The maximum measured groove depths were also only found to be approximately 35% of the grid thickness, whereas the prior model had predicted erosion up to 75% after 36 kh of operation of the LDT throttle profile. As mentioned above, updated modeling efforts to capture the post-LDT observations and analysis are underway and will be presented at a later time.

A2. Accelerator grid barrel erosion aperture enlargement

Barrel wall erosion of the accelerator grid apertures will eventually enlarge the opening to an extent where electron backstreaming is no longer adequately prohibited. NEXT was designed to reduce aperture enlargement by starting with larger diameters and reducing the beam current densities. No significant decrease in the electron backstreaming margin was measured over the course of the LDT.[3] While improvements in the NEXT design to maintain the grid gap distance also contributed to maintaining electron backstreaming prevention, the aperture minimum diameters were found post-LDT to have increased only by 5-7% after the deposition was removed.[6] This shows marked improvement in preventing electron backstreaming as a failure mechanism. The prior analysis estimated that accelerator grid aperture enlargement has been severely reduced and significant life beyond pit-and-groove erosion is anticipated.[2]

However, as with the pit-and-groove erosion analysis, ongoing correlation of modeling efforts to assess the impacts of backsputtered carbon deposits and to confirm minimal barrel wall erosion across the entire throttle table will be needed to be completed to confirm the NEXT service life based on this failure mode. As a point of reference, the worst barrel erosion

A3. Accelerator grid rogue hole formation

Irregular and excessive erosion above and beyond the nominal erosion of the accelerator grid is denoted as "rogue" hole formation. These deformed apertures are likely formed by debris or other contamination on the corresponding screen grid aperture, which distorts the local potential field and deflects high energy ions to a certain portion of the accelerator grid aperture wall. It is unclear where this debris originates from, but if it is primarily of facility backsputter content, it is expected that the presence of similar debris generation in a flight environment would be significantly less. Even with long duration operation in the facility environment, only four such rogue holes were found during the LDT.[6] These four rogue holes were found to have no noticeable impact on the ion optics performance. There was no observed loss of electron backstreaming margin. A significantly higher number of rogue holes would be needed to impact thruster performance or even lead to failure. The NEXT thruster incorporates a flake retention mesh in the lining of the discharge chamber to reduce the possibility of such debris migrating to the optics, and as mentioned above, the flight environment will produce less debris in general.

To generate a first-order estimate, the occurrence of a rogue hole formation can be modeled as a random event occurring over time (or here, propellant throughput will be used as an equivalent for duration) through a Poisson distribution. The rate of four rogue holes developing over 918 kg of throughput, as experienced with the LDT, can be used to model the effective rogue hole generation rate. A sample mission throughput of 1000 kg, for example, would expect less than 1% probability of more than 10 rogue holes and less than 0.1% probability of more than 12 rogue holes as seen in Figure 1. As a reminder, these numbers correspond to less than 0.05% of the total number of apertures, and it is not expected to noticeably affect thruster operation or performance. In addition, since rogue hole formation is likely strongly affected by facility backsputter contamination, the rate of rogue hole generation in flight will be significantly reduced. As will be discussed further below during the grid short subsection, the rate in the flight environment may be over two orders of magnitude lower than the observed ground facility environment. In this case, it is likely less than 0.1% that more than one rogue hole will be generated in flight per 1000 kg of throughput. As a rather conservative estimate, the ground facility environment (i.e. LDT) rogue hole generation rate can still be assumed. Even then, over 2650 kg of propellant can be processed before even a 0.1% probability is reached to meet a very soft failure criterion of 0.1% of the total number of apertures being affected.

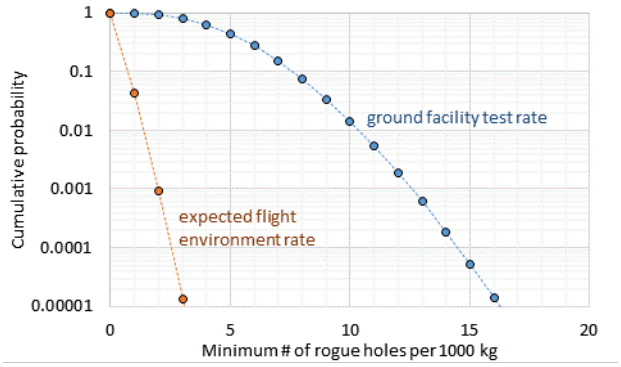

Figure 1: Expected probabilities of rogue hole formation over 1000 kg of throughput

A4. Screen grid erosion

The screen grid optics are in constant contact with the discharge plasma when the thruster is operating, and wear through sputter erosion has been observed. Significant erosion of the screen grid can affect the potential profiles of the optics, the screen grid's ability to shield the accelerator grid, and ultimately its structural integrity. Erosion of the screen grid will also result in redeposition of grid material elsewhere in the thruster, potentially leading to electrical shorts or other failure modes. However, since the screen grid is tied to the discharge cathode potential and the relative plasma potential is relatively low—on the order of 20 – 30 V—erosion of the screen grid is typically minimal and not a significant concern as a life limiting mechanism.

A simple model was created to assess the radial profile of screen grid sputter erosion. There are three main parameters that need to be assessed to calculate sputter erosion, the current density, ion energy, and ion incident angle. These parameters should be calculated for each significant ion population, here the singly, doubly, and triply-charged ions are considered. The total current density profile as a function of radial location is presumed to have the same profile shape as the beam current density. Measured beam current density profiles are available as close as 3 cm downstream of the thruster grids, however, the beam current density profiles directly at the grid location were calculated using ion optics models correlated to the measured downstream data.[7] These profiles are then normalized such that the total current collected by the screen grid is equal to the measured values. The resulting screen grid current density profiles are shown below on the left side of Figure 2.

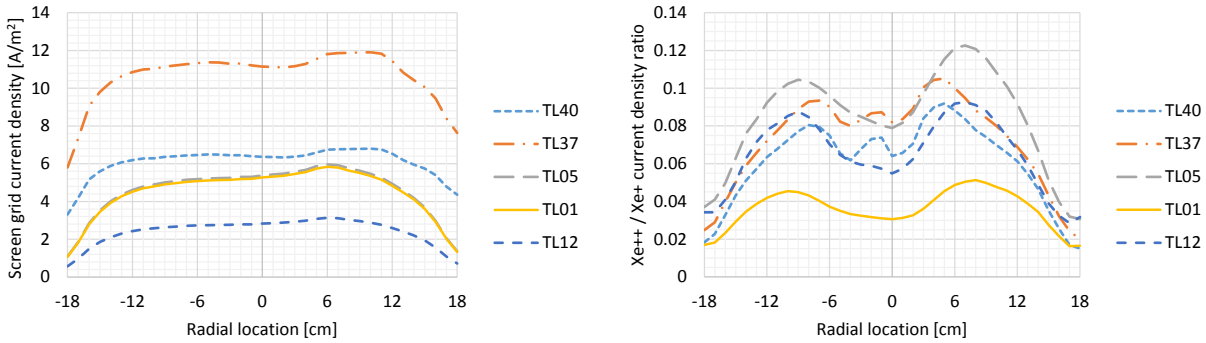

Figure 2: Current density profiles (left) and double to single charged ion ratios (right) at the screen grid

In addition, the total screen grid ion current during nominal thruster operation is estimated via the calculated screen grid transparency,

$$I_{screen} = I_{beam} \frac{1 - \Phi}{\Phi} \tag{1}$$

Here, since current conservation rather than performance is of interest, the screen grid transparency, Φ, is calculated by

$$\Phi = \frac{I_{beam}}{I_{beam_{biased}} + I_{screen_{biased}}} \tag{2}$$

where I_{beam} is in reality the beam power supply current which includes both the true beam current as well as any current collected by the acceleration grid. The biased condition indicates a biasing of the screen grid to approximately 20 V below cathode potential to minimize the electron current contribution. The total ion current to the grids is assumed to be the same whether it is biased or not. The measured screen grid current was observed to increase over the span of the LDT. Deposition in the barrel section of the screen grid apertures was found to decrease the effective aperture diameters and therefore increase the webbing area fraction and ion current collection surface area.[6] For calculating the ion current densities collected by the screen grid, the BOL measured screen grid currents, presented above in Table 3, are used with the BOL current collection area described above.

From these total current density profiles, individual population flux profiles for the singly, doubly, and triply-charged ion species are generated based on measurements of the ion charge state distribution that were made in the downstream plume for both an engineering and a prototype model of NEXT.[8] For comparison to LDT data, which used the EM3 engineering model, the measurements made on EM4 will be used. However, for assessing the general service life of the flight design, the measurements made on the prototype model PM1R will be used instead. Results from PM1R will be shown in the figures in this section except for direct comparisons to LDT data, where EM4 data was used to generate the plots.

The ratio of doubly-charged to singly-charged xenon ions was found to range generally from 2% to over 12% over the NEXT throttle table. In addition, the distributions show an annular profile, where the peak ratio of doubly-to-singly charged ions was found to be 5-8 cm on either side of the centerline as shown in Figure 2. Triply-charged ion current density ratios are also reported and were found to range from 0.005% to 0.05% for a beam voltage setting of

1179 V. Triply-charged ion ratios were not directly reported for other operating conditions, nor were radial profiles provided. However, even a conservative inclusion of the triply-charged ions—implemented as a flat profile at 0.05%—was generally found to contribute less than 1% to the overall erosion at a given grid location, so the resulting end effect of the lack of detailed information on the triply-charged ions can be considered to be minor.

The ion energies impacting the screen grid is assumed to be proportional—based on the ion charge state—to the potential difference between the discharge plasma potential and the screen grid potential. The plasma potential is an unknown parameter, but is generally estimated to be a few volts above the measured discharge voltage for a given operating condition. Direct potential measurements made in a NEXT-type ion thruster show that the plasma potential between the anode magnetic cusps and near the discharge cathode are approximately 2-4 V above the measured discharge voltage whereas the bulk of the volume within the discharge chamber can be a few volts lower.[9] The ion energies then will be dependent on where the ions are created, but a conservative assumption would be to presume the bulk of the ions are generated in the high potential area near anode inter-cusp regions. The plasma potential measurements were made on an earlier laboratory design of the NEXT thruster, but it is assumed here that the general trends between the plasma potential and the discharge voltage remain the same. For the LDT analysis, a discharge plasma potential 3 V higher than the measured discharge voltage is used.

The screen grid is electrically tied to the discharge cathode, but finite resistances do impose a small correction to the relative screen grid potential. During LDT, the screen grid to cathode potential was measured to range from -0.4 to -1.2 V depending on the operating condition as shown in Table 3. The values reported in Table 3 were taken after the diagnostic repair performed towards the end of the LDT. Measurements prior to the repair were generally less than ±0.1 V than the values shown. In all cases it is seen that the screen grid is at a lower potential than the discharge cathode, though the difference is at most on the order of 1 V. These voltages are added to the overall potential drop and ion energy impacting the screen grid. It should be noted for the LDT, a relatively long electrical path was present between the screen grid and cathode common for diagnostic purposes. However, in the flight thruster design, the return path will be significantly shorter, thus a smaller voltage difference will be expected. Using the LDT values, though, provide some conservatism and will be kept in the analysis.

Finally, the calculated erosion rate will depend on the assumed ion trajectories and incident angles. Generally, the potential profile upstream of the screen grid is relatively flat, drawing ions in a direction normal to the upstream grid surface. There is some focusing by the potential profile around the apertures that draws ions towards the aperture centerlines that can cause non-normal incidence impacts. However, in the center of the webbing region between the apertures, the potential profiles should be drawing ions normal to the surface. This is the same region that was observed to have ridges in post-LDT inspection.[6] For simplicity, the measured thickness of the grid at the ridge locations will be used as the main comparison to the analysis where normal incidence is assumed.

The calculated erosion rates, again using the appropriate engineering model EM4 data, are applied to the LDT throttling segment durations and comparisons to post-LDT measured profiles are shown in Figure 3. As mentioned above, the measured ridge location at the center of the webbing in between any pair of apertures is the best point of comparison as it will have more normal incidence ions than the inner or outer edge of the webbing where the potential fields will be more curved. The calculated screen grid erosion is seen to generally overestimate the measured erosion at the ridge locations, particularly towards the outer portion of the grid. However, the maximum measured and modeled erosion depths are within 50% and provide a conservative estimate of the approximate erosion rates of the screen grid.

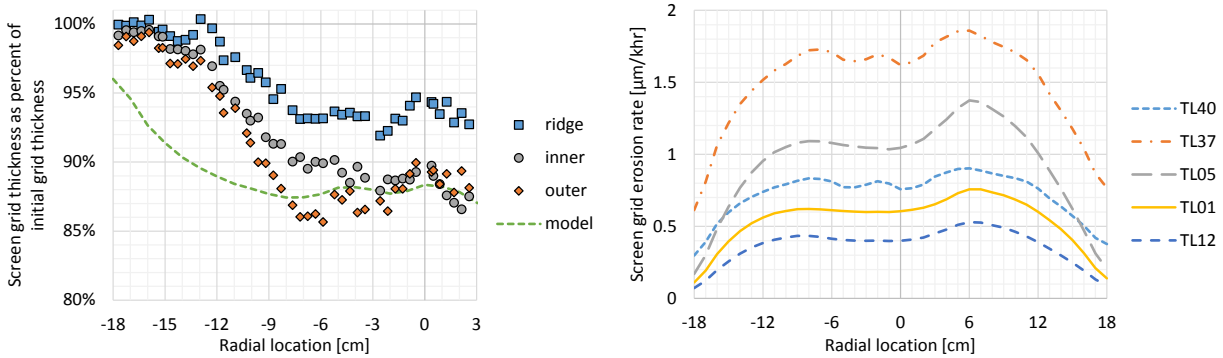

Figure 3: Total screen grid erosion comparison to LDT measured profiles (left) and estimated flight model erosion rates (right)

The flight model erosion rates are calculated in a similar manner, but using prototype PM1R measurements where available. The resulting calculated screen grid erosion rates are also presented above in Figure 3. Throttle level TL37 (1179 V, 3.52 A) has the highest erosion rates, peaking around 2 μm/kh, due to its high current density collected by the screen grid (due to a high beam current with a relatively lower screen grid transparency) and ratio of doubly charged ions. Perhaps surprisingly, TL05 also has a relatively high erosion rate despite a much lower overall current density. The relatively high populations of doubly charged ions are responsible in this case, even contributing more erosion than the singly charged ions at some locations. The high contribution of doubles to the erosion rate is due to the steep drop in the sputter yield at these very low ion energies. Over an order in magnitude increase in the sputter yield is observed for xenon ions around 50 – 60 eV as compared to 25 – 30 eV.[10]

The potential service life limits arising from screen grid erosion will now be addressed. There are several potential failure modes of an excessively eroded screen grid. First, if the webbing material is completely eroded through, the acceleration grid is then exposed to high energy ions resulting in fast erosion of that grid and eventually electron backstreaming. There is also the possible loss of structural integrity of the screen grid if the webbing thickness becomes too thin, leading to mechanical failure and plastic deformation of the optics, potentially including an unclearable grid short. The effective electrostatic pressure on the screen grid during operation at maximum voltage is approximately 180 Pa (0.026 psi). Applying a structural margin of safety factor of 1.4—using NASA-STD-5001 as a rough guide—on this effective pressure then provides an analysis load of 255 Pa.

Two failure conditions are examined here, 1) when the axial displacement exceeds the grid gap distance and 2) when the stress exceeds the yield strength. Analytical solutions from membrane theory for a solid spherical cap with tangential edge support boundary conditions are available for both uniform radial and axial loads and are shown in Table 4.[11] Here, P is the applied load pressure, R is the spherical radius of the cap, θ is the cap half angle, t is the grid thickness, E is the elastic modulus, and ν is the Poisson ratio. To account for the aperture perforations, effective elastic property values, E^* and ν^*, are used instead.[12] In addition, also due to the perforations, a stress intensity factor of $K(D/h)$—where D is the distance between the centers of two adjacent apertures, and h is the minimum width of the webbing between two apertures—is applied to the calculated stress of a solid cap.[13] The factor K is based on the ratio of the radial and tangential stress components. For the radial load case, the two stress components are equivalent and $K \approx 1.15$, while for the axial load case, the stress ratio is equal to $cos(2\theta)$ and $K \approx 1$. Finally, a previously finite-element modeled thermal stress of 11 MPa is superpositioned on top of the plate bending stress, though no additional credit on the limit load is taken, again for conservatism. It should also be noted that the thermally-induced stress in a perforated spherical cap will be highest around the outer radius (where sputter erosion is the lowest) and minimal in the center (where the erosion is the highest), but the maximum stress and erosion are used in the calculation for further conservatism.

Table 4: Maximum displacement and stress for a spherical cap under uniform load[11]

Load direction	Displacement	Stress
Radial	$\delta = \frac{PR^2}{2Et}(1-\nu)(1-\cos\theta)$	$\sigma = \frac{PR}{2t^2}$
Axial	$\delta = \frac{PR^2}{2Et}\left(2(1-\cos^3\theta)+(1+\nu)(1-\cos\theta)\right)$	$\sigma = \frac{PR}{2t^2}$

For all of the load direction and displacement and stress cases examined here, the screen grid is not expected to meet structural failure until less than 0.5% of the initial thickness remains. That is, erosion of 99.5% of the initial thickness is required before resulting in expected structural failure. At the highest level of erosion at the worst-case operating condition (TL37), this would require over 200 kh of operation or an equivalent throughput of over 4100 kg of xenon.

A5. Contamination debris grid shorting

Electrical shorts caused by deposition flakes and other potential contamination debris bridging the two grids are mitigated through both prevention and repair means. Proper implementation of requirements, procedures, and process controls applied at the thruster, subsystem, and spacecraft integration levels will reduce the chances of external foreign debris causing a short. Deposition arising from the thruster that could cause grid shorts can be generally grouped into coming from the grids themselves or from the discharge chamber. Results from post-LDT thruster inspection show

that deposition on the screen grid was minor with little evidence of spalling and subsequent shorting.[6] For the discharge chamber, a flake retention mesh is implemented in the thruster design to retain sputter deposition and to prevent spalling and subsequent flake formation from creating issues elsewhere in the thruster including grid shorts. In addition, the mesh is designed such that if material does spall from the mesh, the resulting flake size should be smaller than the grid gap.

Nearly 72,000 flakes were collected from the discharge chamber post-LDT and were measured.[14] The resulting cumulative distribution of the maximum dimension is shown in Figure 4 along with a fitted Weibull curve with a scale parameter of 9.6 and a shape parameter of 0.47. It is estimated that well below 0.5% of flakes observed during the LDT could potentially bridge the gap and cause a short. Preliminary analysis of the flakes showed characteristics similar to those observed for NSTAR.[15] Some of the larger flakes were semi-circular in form, as seen in the right side of Figure 4, with the diameters indicating origination from the accelerator grid optics and energy dispersive x-ray spectroscopy (EDS) analysis also indicating primarily grid material content. Other large flakes were found to have a two or three layer formation with one or more of the layers consisting of primarily carbon from facility backsputter.

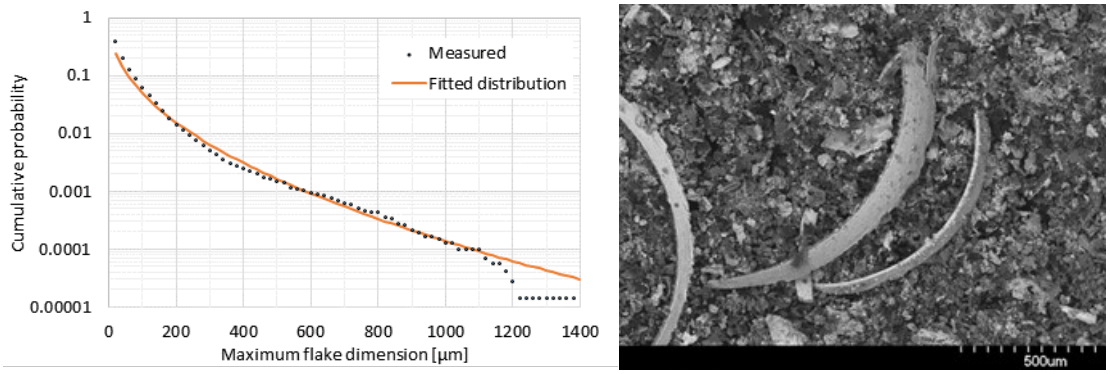

Figure 4: Cumulative probability of post-LDT measured flakes with maximum dimension (left) and image of sample flakes (right)

During the LDT, nearly 40,000 thruster recycles were observed, generally averaging a little under one per hour as seen in Figure 5. These recycle rates were generally in line with past observed rates for NSTAR ground testing. Generally recycle events were more prevalent during higher beam current operation, particularly during transitions to those operating conditions around 265 kg and 475 kg of throughput in Figure 5 below where differences in erosion patterns and thermal conditions may have created a temporary increase in flake generation. All of these recycle events over the course of the LDT were successful and no persistent grid short was observed. The ground test facility environment, likely due to the presence of facility carbon backsputter, has been seen to incur a much higher recycle rate than in flight. While the ground-based testing of the NSTAR thruster observed upwards of 60 recycle events per kilogram of xenon throughput, in-flight observations of the DAWN mission have reported less than one recycle event per kg per thruster over total throughputs of 95 – 155 kg of xenon equivalent to 9.5 – 19.9 kh of operation.[16] Recycles were even less prevalent for Deep Space 1 (DS-1). This is a reduction of over two orders of magnitude of the frequency of recycle events from ground testing to in-space conditions as seen in

Table 5.

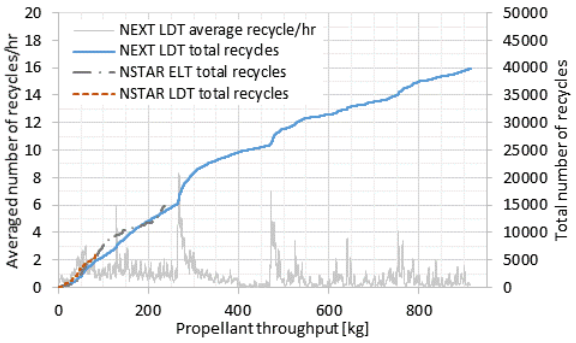

Figure 5: Thruster recycle events during LDT

Table 5: Average recycle rates for flights and tests

Case	Average recycle rate
DS-1 (flight)	0.25 recycles/kg
DAWN (flight)	0.46 recycles/kg
NSTAR LDT (test)	71 recycles/kg
NSTAR ELT (test)	63 recycles/kg
NEXT LDT (test)	52 recycles/kg

In the case where a flake or other debris is present and creating a grid short situation, there are several options to rectify the issue. As described above, during the LDT many instances of low impedance between the grids were successfully cleared upon a normal thruster recycle event or during thruster warmup. If the thruster continually recycles, then mechanical means to remove the shorting material, such as thermal soaking to open the grid gap size, is recommended. As the thruster heats up from a cold condition, the screen grid will warm up and expand first, then the accelerator grid. Analytical calculations and finite element modeling of grid thermal expansion have shown expected displacements on the order of 100 μm for grids of comparable size,[17] which is a significant fraction of the nominal grid gap distance. A final means to try to clear a stubborn grid short is the use of a grid clearing circuit as is implemented in the NEXT power processing unit.[18,19] The circuit has the capability to apply the discharge supply up to 24 A across the screens to vaporize or ablate foreign material from between the grids. Analysis and testing of the current required to clear flakes and wires of various sizes showed that 10 A would be sufficient to clear the larger molybdenum flakes recovered from NEXT 2000 h wear testing.[18] In summary, the occurrence of grid shorts due to contamination debris is expected to be much lower in flight and several mitigation schemes are present to clear them.

III. Discharge Chamber

B1. Magnet overheating

High temperatures can cause irreversible magnet degradation and lead to loss of field strength and subsequent thruster failure or reduced operation. A temperature limit of 360 °C is imposed for the NEXT magnets. This results from a 40 °C margin, the same margin used for NSTAR, applied to the magnet stabilization temperature of 400 °C. Temperature measurements of the engineering model EM1 showed peak magnet temperatures at 303 °C, while measurements of the prototype model PM1 had a peak magnet temperature of 272 °C with an external applied environmental heat load.[20,21] These measurements show there is over 50 °C margin even at the worst thermal conditions. Characterization of the magnets show excellent long-term stability at elevated temperatures around 300 °C.[22] Indeed, measurements of the magnetic field before and after the LDT did not reveal any significant changes. The stability of the discharge performance over the course of the LDT further demonstrated that magnet overheating and degradation is not expected to be a critical wear mechanism for NEXT.[14]

B2. Electrical isolation and insulation loss

Electrical isolation and insulation is a critical aspect to ensure successful thruster operation. In addition to potential grid shorts as described above, other areas requiring proper electrical isolation or insulation include the propellant isolators for the cathodes and the main plenum; the electrical stand-offs between the anode, grids, and cathodes; and the wiring insulation. Best practices in isolator design were implemented to prevent issues seen in the past with older isolator designs.[23,24] An early component-level verification test of the high voltage propellant isolator (HVPI) demonstrated over 18 kh of operation at an elevated temperature 65 °C above the worst case expected flight temperature.[25] This was followed by full life testing of the HVPIs, which demonstrated over 51 kh of operation, again with the 65 °C margin elevated temperature. The maximum leakage current was measured to be 2.4 nA, which is orders of magnitude below the test's 100 μA criterion. Then, over the 50 kh of the LDT, none of the HVPIs exhibited any signs of leaks, impedance issues, or arcing over the course of the test and the post-test inspection.[14]

The low voltage propellant isolator (LVPI) on the neutralizer cathode did show loss of impedance during the LDT arising from deposits on the insulator.[14] It should also be noted that while undesirable, the lower impedance observed during the LDT did not result in thruster failure nor even a noticeable change in measured performance. The cathode to ground potential did not exhibit any significant changes over the course of the LDT either. The deposits were found to consist primarily of the insulator fitting material constituents. It is suspected that arcing events led to ablation of the fittings around the insulator, as signs of localized melting and pitting of the upstream lock fitting and the downstream seal fitting were observed. The arcing is speculated to occur during thruster recycle events where a relatively dense plasma will be present within the neutralizer cathode. However, these arcing events occurred with an engineering unit design which has a plasma screen with a relatively high open area fraction as seen in the left side of Figure 6. The flight-like thruster design, on the other hand, has an optically dense plasma screen as seen on the right side of Figure 6. The mesh will prevent charged particles from entering the LVPI and initiating arcing events. Indeed, results from testing of the flight-like NEXT design with the flight LVPI has over 2000 h of operation without any signs of arcing or impedance degradation.[26]

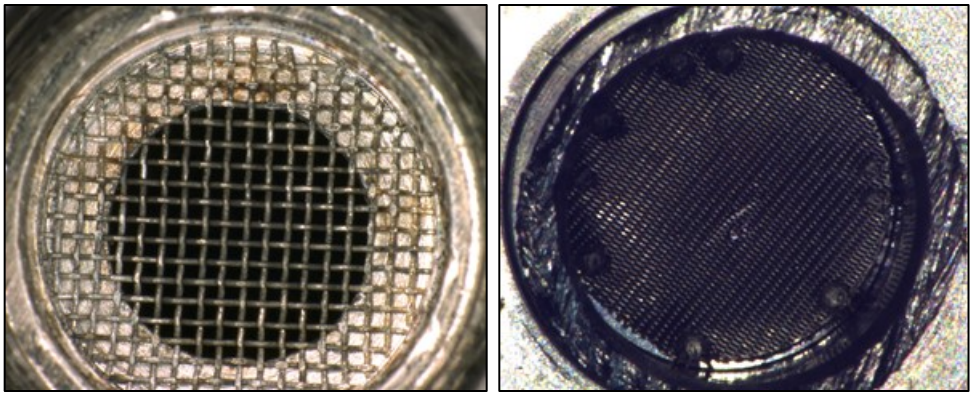

Figure 6: The low voltage propellant isolator plasma screen for engineering unit (left) and flight unit (right)

The neutralizer cathode main isolator, between the keeper and cathode, was observed post-LDT to have tiny spherical debris near the outer edge. Material analysis confirmed that it consisted of the braze material. The debris was minimal, however, and keeper-to-cathode impedance was not advserely affected during and after the LDT. Debris was also noted within the ion optics mounting insulator shadow shields, but not on the insulators themselves. Some discoloration was present on the optics insulators, but was easily wiped off. The grayish discoloration is suspected to be back-sputtered carbon dust from spalling from exposure to atmospheric pressure. The impedance for each optics isolator from the LDT was checked and no degradation was measured. Similarly for the gimbal, DCA, and NCA mount insulators, no impedance issues were observed. The mount insulators for the gimbal and both cathodes had some superficial metallic contact rubbing marks from assembly/disassembly were noted.

Within the discharge chamber, sputter-deposited film buildup creating a conductive path across isolator surfaces is a potential concern. However, shadow shielding and other design aspects are implemented to remove this as a potential concern. Most of the discharge chamber isolators inspected after the LDT were found to be clean with no signs of arcing or of impedance degradation. The one exception was the screen grid wire as it passes through the anode. Sufficient deposition—characterized to be carbon from the facility—was found to reduce the impedance between the screen grid and anode. Again, though this issue was found for the engineering design model tested in the LDT, due to the perforated plasma screen enclosure, it will not be an issue for the flight design which will use a solid enclosure preventing sputter deposition from accessing the region of issue.[14] In addition, there will be no facility backsputter deposition in space to create the conductive coating to bridge the separation. After the LDT, all of the wiring within the thruster was inspected with the fiberglass sleeving removed. No impedance degradation was measured.

IV. Discharge Cathode

C1. Keeper erosion

One of the key functions of the DCA keeper is to protect the cathode orifice plate and external heater from bombardment of energetic ions that may limit the lifetime of the cathode. While a loss of the keeper does not result in thruster failure, predicting the lifetime of the keeper is necessary to ensure sufficient life of the cathode. Experimental and analytical investigations were, therefore, conducted in the past to predict the wear of the discharge cathode keeper in the NEXT thruster. The NEXT molybdenum discharge keeper had been analyzed based on the NSTAR extended life test to estimate its lifetime using deterministic and statistical approaches.[27] Although the assessment showed that the keeper should last a minimum of 375 kg of xenon throughput and possibly up to 844 kg, higher than anticipated keeper wear was observed during the NEXT 2000-hour wear test.[28] As a result of the wear test, the discharge cathode keeper material was replaced with graphite to achieve longer life, which has a significantly lower sputter yield as compared to molybdenum.

A semi-empirical keeper erosion model was developed in order to evaluate the angular impacts of ions on the NEXT discharge cathode keeper surface and estimate its lifetime.[1] Since details of the model have already been previously discussed, only key assumptions are reviewed in this paper. In this semi-empirical model, the ions eroding the keeper are assumed to originate from an effective point source. Although this assumption is just a first-order approximation, a measurement shows that the ion distribution was highly peaked toward the keeper orifice[27] and the model can predict measured wear patterns and rates reasonably well.[1] Another key assumption of the model is that the

erosion profile of the keeper surface is based on the angular sputter yield of the point ion source. The magnitude of the normal sputter yield and location of the ion point source are determined by fitting to experimental keeper wear profile data. Other assumptions include using a constant ratio of double to single charged ions. This model was used first to predict the wear rates of the NSTAR molybdenum discharge cathode keeper, which were compared with 8200-hour wear test.[29] The model prediction showed a reasonable agreement with the wear test profile. The model was then used to predict the wear for the NEXT molybdenum keeper. A good agreement was seen between the model prediction and the profilometry data of the NEXT molybdenum discharge cathode keeper taken after its 2000-hr wear test.[28] These agreements show that the model can serve as an adequate analytic tool to predict the wear profile of the keeper.

The same model was used to estimate the NEXT graphite keeper wear profile for the LDT. The LDT throttle profiles and durations, which were summarized above in Table 2, were input into the model. Since the model was built based on the assumption that the angular dependence of the sputter yield is an important factor influencing the wear pattern of the keeper surface, some discussion on the angular profile for graphite sputter yields is provided here. Figure 7 shows experimentally measured angular sputter yield data of graphite at various incident energies.[30-33] The relative spread of yield values at similar ion energies and of profile shapes across incident angles highlights the uncertainties present in the data and yield values. Here, a Bayesian analysis approach can be used to calculate best fits to the available data.[34] The angular dependent portion of the sputter yield, Y', is assumed to follow a two parameter $(\beta/\alpha,\ a/\alpha)$ fit as formulated by Wei,[35]

$$Y'(\theta) = \frac{1}{\sqrt{1+(\beta/\alpha)^2\tan^2\theta}}\exp\left(\frac{1}{2}\left(\frac{a}{\alpha}\right)^2\left[1-\frac{1}{1+(\beta/\alpha)^2\tan^2\theta}\right]\right) \quad (3)$$

A Markov chain Monte Carlo nested sampling routine is used to calculate the two parameters based on the available graphite angular sputter yield data, and best fit values of $\beta/\alpha = 0.9,\ a/\alpha = 2.2$ are found and the resulting curves plotted in Figure 7. These angular profiles are then used in the keeper erosion model. The magnitude of the normal sputter yield and location of the ion point source are then used as fitting parameters to match the measured 50 kh NEXT LDT keeper wear profile as shown below in Figure 8. The post-LDT profilometry measurements of the keeper surface profile shows that the maximum depth eroded is 16.5% of the total thickness of the keeper orifice plate, which is observed at a radial location approximately one orifice diameter from the centerline.

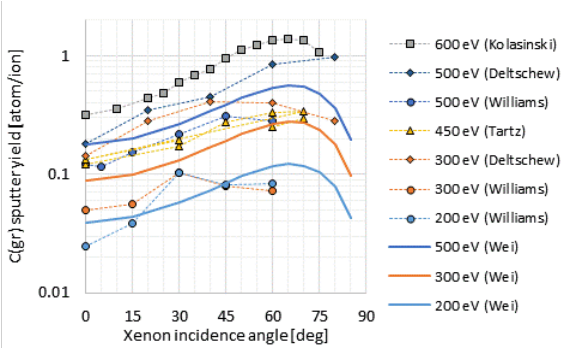

Figure 7: Angular-dependent sputter yields of graphite from xenon bombardment[30-35]

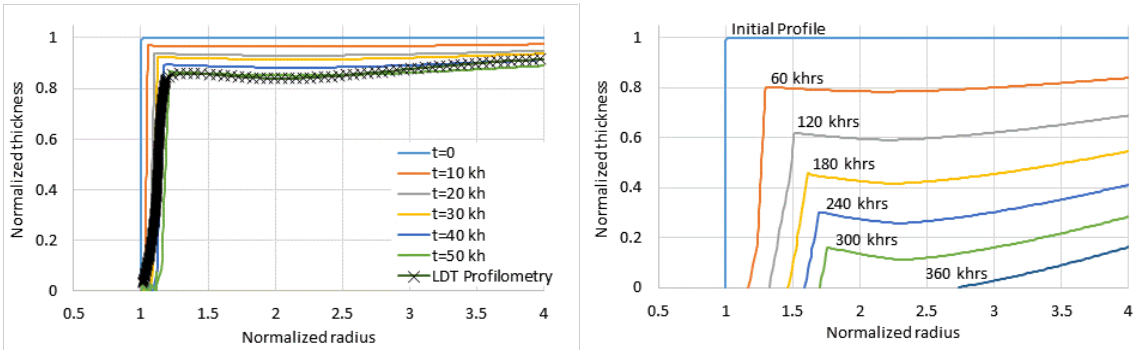

Figure 8: Modeled wear of the graphite DCA keeper for the LDT (left) and eventual failure (right).

In the model, the amount of ion current from the point source is dictated such that the sum of the model's keeper ion current is equal to the measured ion keeper current.[1] The model takes the corresponding keeper current, as provided in Table 3 for the LDT, for a given amount of time to calculate wear profiles. The keeper draws more ion current when the beam current is high and beam power supply voltage is low, making the TL37 condition to be the worst case throttling condition for keeper wear. Therefore, the TL37 condition is used to make a conservative estimate of the lifetime of the keeper. If we define the soft failure of the keeper as when the keeper has been eroded as to expose the cathode heater to discharge chamber plasma, then its lifetime is estimated as shown in Figure 8. The model predicts that the keeper would erode to expose the heater after approximately 333 kh of operation, which corresponds to 6900 kg of xenon throughput, using the worst case throttling point and the BOL total mass flow rate. This result is based on the model assuming a fixed point source for ions. However, there exists the possibility the keeper could erode faster as the ion current opens up the orifice region faster.[1] Therefore even as a conservative estimate where the keeper is assumed to wear at twice the rate of the worst case throttling condition, 3500 kg of throughput would be required before it exposes the discharge cathode heater to plasma. Even then, this is only a soft failure criterion. The NSTAR discharge cathode keeper orifice plate was observed to completely erode away during its extended life test, but this did not immediately preclude operation and subsequent ignitions of the cathode and thruster; indeed over 15 kh of thruster operation was successfully run with the cathode heater and orifice plate fully exposed without any subsequent measurable change in the ignition voltage or duration.[36]

C2. Cathode orifice plate erosion

One of the primary functions of the cathode keeper is to protect the rest of the cathode from ion impingement erosion. As the keeper experienced only relatively minor erosion over the course of the LDT, much of the cathode orifice plate also remained intact. Erosion of the orifice plate was only observed in the regions not shielded by the keeper; it was otherwise nearly pristine.[26] The downstream corner of the orifice chamfer experienced the highest amount of erosion for the cathode orifice plate, but it was still at a lower rate than the keeper erosion described above. The cathode orifice plate was seen to erode in this location by approximately an average of 6 μm/kh. As will be further discussed below in the deposition subsection, there is evidence this erosion occurs at least during high current operation, though it doesn't preclude erosion at lower current operation as well. Assuming worst case that the erosion is only significant during high current operation, then an effective erosion rate of over 7 μm/kh may be present. Even at this rate, the orifice should survive over 3400 kg of throughput, or over 160 kh of operation.

For the discharge cathode, net deposition was observed on the orifice barrel section during the LDT. The deposits were found to be of the same material as the orifice plate itself. Since the deposition was not found to be from facility back sputter or another facility effect source, net deposition is expected to occur in flight as well and direct erosion of the barrel section of the discharge cathode orifice is not a concern. Further details are discussed in the following subsection.

C3. Keeper and orifice plate deposition

As with erosion discussed above, the discharge cathode orifice plate has the same two primary areas of potential concern with deposition, the downstream face and the orifice barrel section. Beginning with the latter, deposition was observed on the barrel portion of the discharge cathode orifice from the LDT. Post-test examination found that the diameter of the orifice was reduced by approximately 13% due to accumulated deposition.[26] This correlates to an average deposition rate of 2 μm/kh. Based on composition analysis, the deposited material was found to be primarily from the orifice plate itself, likely from the downstream portions that exhibited erosion. A simple model was created to simulate the erosion and subsequent re-deposition within the DCA orifice region. The COLISEUM code was repurposed to model the NEXT DCA orifice region.[37] A simple point source ion beam was assumed as for the keeper erosion model above. The Yamamura formulations of the sputter yield and ejected sputter product distribution were used to calculate the erosion rates and resulting redeposition rates on the various surfaces based on the view factors present in the orifice region.[38-40] The resulting erosion and deposition rates are shown in Figure 9. The erosion of the orifice chamfer region is consistent with the rates estimated above and the resulting deposition rates in the orifice barrel region are found to correlate well with the LDT observations. This further supports the theory that the barrel region deposition is primarily sourced from the chamfer region eroded products. With a deposition rate on the order of 2 μm/kh on the inner barrel region, over 400 kh would be required before the orifice diameter is reduced even by half. In addition, as the orifice closes, the current density of the discharge cathode plasma will also likely rise leading towards a competing erosion process, as was seen for the small diameter NSTAR neutralizer cathode.[41] Thus, as previously expected, orifice clogging is not a life limiting concern for the DCA.

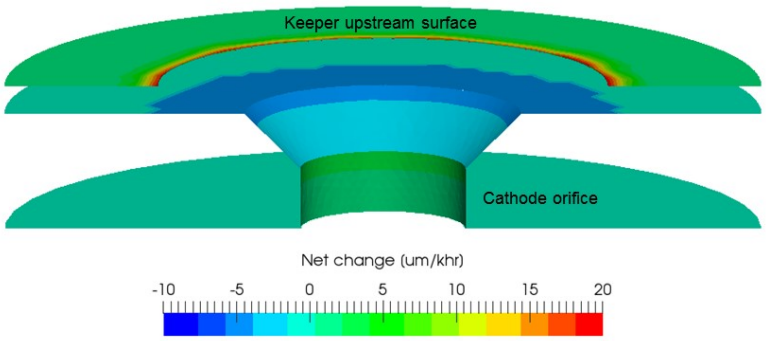

Figure 9: Sputter erosion and redeposition model results of DCA orifice and keeper

The downstream cathode face generally experienced net erosion during the LDT as noted in the previous subsection. However, a deposition ridge was observed during the post-test inspection.[26] Deposition was also observed on the upstream surface of the keeper orifice. As with the barrel deposition, these deposits were also found to be the same material as the orifice plate and it is presumed that the sputtered material from the orifice plate re-deposited on the keeper upstream surface and eventually grew upstream towards the orifice plate. It is speculated that eventually a bridge formed between the cathode and keeper and likely broke in the middle later during thermal cycling to leave the ridge on the cathode side. This theory is further supported by observation of net erosion radially outside of the deposition ridge on the orifice plate. Growth in material deposits on one or both sides led to a reduction in the cathode to keeper gap and enhanced the likelihood for an electrical short between the two. Indeed, intermittent electrical shorts were observed between the discharge cathode and its keeper during the LDT starting after approximately 13.8 kh of operation (265 kg of throughput) as seen in Figure 10.[26] The shorting events were primarily noted to be thermally induced, but a more consistent cold short was noted after approximately 48 kh (~850 kg) of the test. The average deposition rate required to bridge the cathode to keeper gap at operating temperatures is approximately 22 μm/kh. This is in general agreement with the results of the prior 2000 h NEXT wear test, which observed a deposition of 40 μm in the same location after 2000 h of full power operation, or an average deposition rate of 20 μm/kh.[42] This growth rate is also matched with the model results shown above in Figure 9, further supporting the presumption that the source material is primarily from the orifice plate. Note that it is also peaked at just the inner radius of the keeper orifice, which also matches the observed growth ridge location.

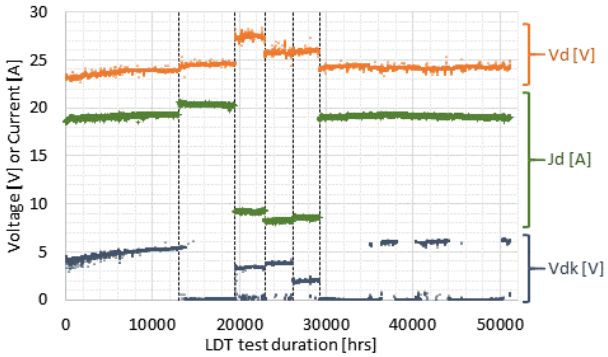

Figure 10: LDT discharge voltage (Vd), current (Jd), and discharge cathode to keeper voltage (Vdk)

Three potential issues can result from DCA keeper to cathode shorting. The first is increased keeper erosion due to an increase in potential drop and resulting ion impact energy, but as described above, even accounting for the shorted condition over a third of the duration of the LDT, the keeper erosion is still relatively low and not a driving life limiter. The second potential issue from keeper to cathode shorting are discharge extinguish events. Sixteen discharge extinguish events were observed during the LDT, as shown in Table 6, and all of them occurred with the DCA keeper shorted to the cathode before or during a thruster recycle. The extinguish events are primarily observed during low current operation, even though the relative occurance of shorted recycles per propellant throughput is notably lower than for high current operation.

Table 6: Discharge extinguish events during the LDT

Throttle segment	Throttle level	Operating condition	Segment throughput	Segment recycles	Recycles with short	Extinguish events
1	TL40	1800 V, 3.52 A	265 kg	15391	0	0
2	TL37	1179 V, 3.52 A	132 kg	9140	5411	0
3	TL05	679 V, 1.20 A	26 kg	515	111	10
4	TL01	275 V, 1.00 A	22 kg	388	24	3
5	TL12	1800 V, 1.20 A	24 kg	505	4	1
6	TL40	1800 V, 3.52 A	445 kg	13218	9225	2

These event statistics from the LDT can be used to generate probabilities of a discharge extinguish event occuring for a mission. One approach is to model the number of extinguish events, k_e, per the number of shorted recycles, k_s, as a binomial distribution with a probability q_e based on the LDT data in Table 6 for a given operating condition. The number of cathode-keeper shorted recycles per number of total recycle events, k_r, can be modeled in a similar fashion with probability q_s, also based on LDT results. Finally the number of total recycles per propellant throughput, t, may be described via a Poisson distribution with a recycle rate of λ_r. As noted previously, during the discussion of grid shorting events, the number of thruster recycles in flight are substantially lower than in ground test, as shown before in

Table 5. For the analysis here, the DAWN recycle rate of 1 recycle per 2.2 kg of throughput will be assumed as a starting baseline. Then the various probability distributions can be chained together to provide an estimated distribution of discharge extinguish events for a given propellant throughput:

$$P(k_e) = \sum_{k_s=0}^{\infty} \left\{ \binom{k_s}{k_e} q_e^{k_e} (1-q_e)^{k_s-k_e} \cdot \sum_{k_r=0}^{\infty} \left[\binom{k_r}{k_s} q_s^{k_s} (1-q_s)^{k_r-k_s} \cdot e^{-\lambda_r t} \frac{(\lambda_r t)^{k_r}}{k_r!} \right] \right\} \tag{4}$$

The probability of at least one extinguish event per kg of throughput for a single thruster at a single operating condition and are shown below in Figure 11. It should be noted that this already assumes the thruster has operated sufficiently long enough to establish a discharge cathode to keeper short, which again, for the LDT required over 265 kg of propellant processed at high current operation. So the throughputs shown in Figure 11 are on top of an initial 265 kg. Another note of the analysis regards the probabilty q_e for the TL37 operating condition. Since no extinguish events were observed over throttle segement 2 for the LDT, the strict interpretation is a zero probability. However, as a worst-case bound, let us assume there was one extinguish event encountered instead of none. The resulting probabilities are then similar to the TL40 operating condition as seen in Figure 11, though again, this is a hypothetical upper bound.

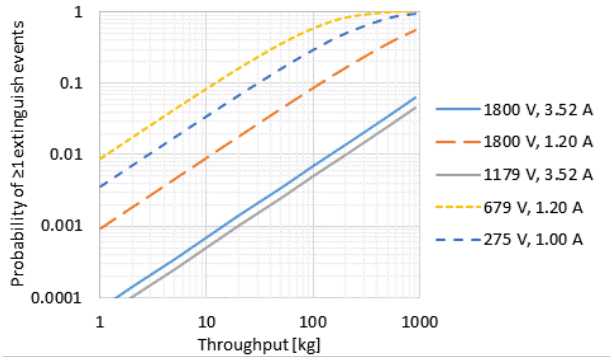

Figure 11: Cumulative probabilities for at least one discharge extinguish event for a given operating condition as a function of throughput

It should be clearly highlighted, in any case, that the occurance of a discharge extinguish event is not a life-limiting failure for the NEXT thruster. Indeed, the thruster was successfully restarted for all occurances over the course of the LDT. Should a discharge extinguish event happen in flight, the digital control interface unit (DCIU) which controls the PPU and propellant management system can be programmed to restart the thruster without ground intervention as was done for NSTAR as a mitigation approach. In addition, it is speculated that the additional reduced impedance between the anode and the screen grid may also exacerbate the likelihood for an extinguish event to occur. In this case, an extinguish event is further unlikely to occur in flight as the mechanism for reduced impedance between the anode and screen grid during the LDT was caused by ground facility backsputter deposition and without the fully enclosed shielding of the flight design thruster.

Finally, the third issue with cathode to keeper shorting events are potentially longer cathode ignition times.[3] Approximately 36% of ignitions during an observed short required more than the nominal six minutes.[26] A separate study with the EM4 thruster during algorithm validation testing was conducted with intentional shorting of the discharge keeper to the cathode. Here, an average ignition time increase of approximately two minutes over nominal was observed, which is comparable to what was seen during the LDT. Correspondingly, the NEXT DCIU is programmed to attempt cathode ignitions for up to 30 minutes and to repeat the 30 min heater durations twice more if needed. Though increased ignition times are not ideal as they limit the responsiveness of the system to ignite on demand, a cathode-to-keeper short has not been observed to be a thruster failure or life-limiting mechanism with all 350 ignitions for the LDT resulting in successful ignition. No indications of a short based on ignition time have been observed to date for DAWN, where 679 ignitions have been successfully performed within one second of ignition command after a consistent six minute preheat.[16]

C4. Barium insert degradation

Proper operation of hollow cathodes requires a low work function at the emitting surface to sufficiently supply electrons at sustainable temperatures. Both the discharge and neutralizer hollow cathodes for NEXT are dependent on barium and barium oxide at the emitting surface to provide this low work function. The barium is supplied by barium calcium aluminate ($BaO\text{-}CaO\text{-}Al_2O_3$) impregnated into the voids of a porous tungsten insert within the cathodes. In a simplified sense, the emitter life is governed by the process of barium on the surface of the emitter gradually evaporating and being replaced via diffusion of barium further within the insert to maintain low work function surfaces, with an eventual depletion of available barium. The detailed reality, however, is that there are several other competing processes that both help and hinder the transport of barium to and from the emitting surfaces. Transport of evaporated barium within and through the cathode internal plasma can redeposit the barium on an emitter surface, effectively recycling it for further electron production. On the other hand, transport of tungsten can lead to clogged pores and subsequent reduction of barium diffusion through the insert. Decomposition of the impregnate, impurities in the working gas, or contaminates from the external environment can also react with the tungsten and produce stable barium tungstate formations, effectively locking the barium from further transport and electron production. This subsection will first examine barium depletion as a life-limiting mechanism and then later provide an evaluation of barium blockage or locking as a life-limiting mechanism.

In the previous service life assessment, two approaches towards modeling this barium depletion within the discharge and neutralizer cathodes were presented.[1] The first is a simplifying generalization bounding case of a related planar dispenser cathode. The second delves deeper into the specifics of the operation of the hollow cathode configuration including thermo-chemical processes.[43] Since then, further advances in cathode life and barium diffusion and transport modeling have taken place. Of note, the transport and redeposition of barium has been shown to have an important effect on extending the effective life of a hollow cathode. This effect has been inadvertently observed in planar dispenser cathodes where the presence of a close spaced parallel plate diode (CSPPD) has shown to result in improved robustness in performance and life, whereas without a CSPPD, as in a traveling wave tube configuration, or with an open mesh CSPPD, the life and performance of the dispenser cathodes were found to be diminished in comparison due to reduced barium recycling through redeposition.[44] The importance of barium transport and redeposition has also been modeled specifically for hollow cathodes, where the closed cylindrical geometry inherently provides an environment where barium recycling is prevalent.[45,46] The effect of barium transport and redeposition is even sufficiently pronounced such that tungsten transport and deposition effectively sealing the downstream surfaces of the emitter from barium diffusion—or perhaps equivalently tungstate formation preventing barium diffusion—does not directly result in cathode failure if upstream portions of the cathode are still able to provide a source of barium. This was demonstrated in an extreme case where up to half of an insert was replaced by a pure tungsten matrix without any impregnate and the remaining upstream impregnated insert half was still able to ignite and sustain cathode

operation.[47] Based on these developments, barium depletion is not expected to be a critical life limiting mechanism for the cathodes.

For completeness and due diligence, a reasonably conservative worst-case scenario can still be examined to provide confidence in the ability of the cathode to meet NEXT service life requirements. Following the preliminary NEXT service life assessment, barium depletion based on a planar dispenser cathode geometry can be used as a conservative first-order life estimate where no redeposition or recycling of barium is assumed—once the barium evaporates, it is assumed to be completely lost. Perhaps the simplest phenomenological model that can be constructed under these assumptions is a simple depletion rate based on measured depletion depth data for dispenser cathodes with the form

$$\delta = A\sqrt{t} \tag{5}$$

where the depletion depth, δ, increases with the square root of the total time, t, of operation.[48,49] The time to reach a certain depletion depth, then, is proportional to the square of the rate factor, A, which can be expressed as an Arrhenius-type function of the insert temperature.[46,50] Based on the particular test data set, however, the square of the rate factor can vary by a factor of two or three over the range of temperatures the data are based on as shown on the left side of Figure 12. More importantly, it can be seen that the sensitivity of the depletion rate to the insert temperature is significant, a temperature change of 100 °C can result in nearly an order of magnitude effect on the depletion time.

The DCA insert temperatures were measured in a separate test using an optical pyrometer method and the orifice plate temperature is measured directly with a thermocouple as has been performed for other cathodes.[51,52] The cathode temperatures are primarily dependent on the discharge current. Measured maximum and average values of the discharge current for the five primary throttle levels during the LDT are available in Table 3. The spread of the discharge current values for a given operating condition are in line with assessed dispersions from data analysis across different individual NEXT thrusters and test facilities.[53] Here, the worst-case operating condition, TL37, has a discharge current value around 20.8 A. The peak measured DCA insert temperature is under 1050 °C while the orifice plate temperature is about 100 °C cooler. The peak insert temperature is near the downstream end and drops relatively rapidly going upstream.

Another point of consideration for the above analysis is the defined end of life with respect to barium depletion. The prior assessment above used a limiting depletion depth of 500 μm based on examination of the NSTAR thruster discharge cathode insert from its 30 kh ELT.[1,54] EDS analysis was performed on the NSTAR DCA after the ELT to gauge the relative concentrations of barium and tungsten for worn and pristine insert samples. The depth where the measured barium to tungsten ratio meets the pristine coupon levels is assigned as the depletion depth. A maximum depth of approximately 400 μm was estimated from the few axial locations examined.[54] However, the data shown in the report appears to have significant scatter and it is difficult to place much confidence in the values. The cathode was still successfully operational, so it was presumed that depletion of up to 400 μm, a little over half of the full insert thickness, does not have a notable deleterious impact on cathode operation or performance. Other experimental observations of similar S-type (4:1:1 impregnate) planar dispenser cathodes have also shown depletion depths in the hundreds of microns without failure, though reductions in the space-charge limited current were observed as the barium depleted and another definition of end of life for these dispenser cathodes is provided as a 25-30% reduction in the space-charge limited current.[48] In that work, Palluel and Shroff show a close correlation of current reduction and depletion depth. A 10% reduction in the current can be correlated to a depletion depth of approximately 180 μm. To reach a 25% current reduction then, would correspond to a depletion depth of 450 μm, which is coincidentally similar to the limits previously used.

Using Eq. (5) as described above, the time to reach a depletion depth of 450 μm can range considerably as seen on the right side of Figure 12 depending on the particular temperature and depletion rate factor assumptions. Even with the worst-case assumptions (e.g. TL37 operating condition, 1050 °C insert temperature, higher depletion rate), over 2750 kg of throughput (or over 130 kh of operation) can be expected. Again, the true conditions within a hollow cathode lead to barium recycling that greatly reduces barium loss and depletion. In addition, the barium partial pressure has even been modeled to be higher than the equilibrium vapor pressure for the upstream portions of the insert, further suppressing barium depletion rates.[46] Again, even assuming complete loss or blockage from tungstate or other oxide formation of up to half the emitter surface, the upstream portion (typically at a cooler temperature even) is more than sufficient to provide the barium to maintain cathode ignition and operation performance. In addition, the cathode the cathode will operate at lower discharge currents for all other throttle conditions, and the temperature profile axially along the insert will only be cooler further upstream.

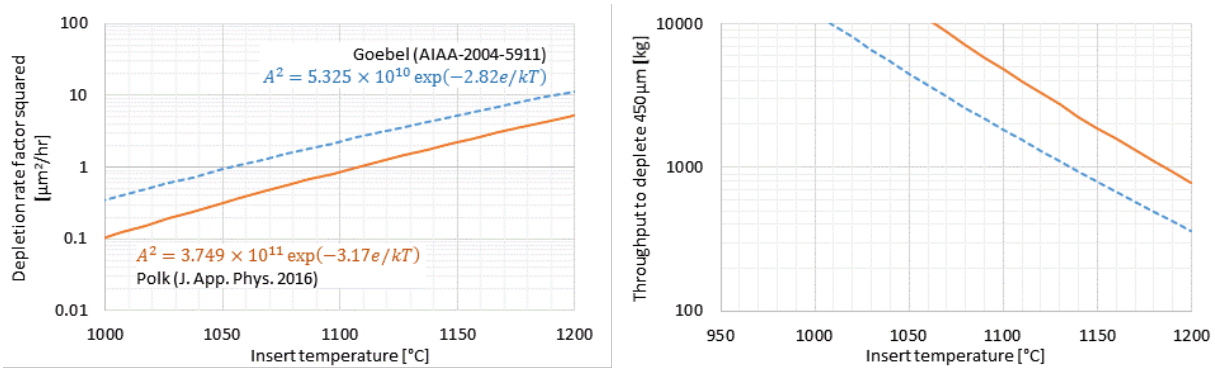

Figure 12: Barium depletion rate factors (left) and throughput (based on TL37 flow rate) to deplete 450 μm of barium (right)

The DCA inserts from the LDT were sectioned and examined to assess the state of the emitter after over 900 kg of throughput. In addition, unused inserts were also sectioned, mounted, and polished at the same time as the LDT insert examination. The unused inserts are of the same batch of inserts used for the LDT, but they were never tested and stored sealed in the original packaging. To assess the barium depletion depth, the chemical content of filled pores and the relative values of barium to aluminum were measured via EDS measurements.[55] This is slightly different than what was performed for the NSTAR cathode post-ELT analysis where the barium to tungsten ratio was examined. Since the EDS measurement can be sensitive to the field of view and depth of the impregnate, the relative quantity of tungsten can vary significantly based on instrument positioning. This technique was meticulously applied to a high number of pores at various axial and radial locations within the inserts, and sample results are shown in Figure 13. The EDS intensity data was fit with a standard-less ZAF (atomic number, absorption, fluorescence) correction to estimate BaO and Al_2O_3 wt% content, based on Ba and Al intensity. A lower barium content near the inner radius can be noted at the 0.5 mm axial location for a radial location less than 100 μm from the inner radius of the non-etched portion of the insert. Similar trends were seen up to a 5 mm axial location—where the relative barium concentration was lower for radial positions less than 100 μm from the inner radius—however at 10 mm and above, no such depletion is noted. From strictly the depletion depth argument, the post-LDT insert shows more than sufficient life remaining even after over 900 kg throughput of LDT operation as no noticeable relative depletion is observed at depths greater than 100 μm, well under the imposed 450 μm limit set above. Based on these measured depletion depths near the downstream end of the insert, the temperature at that location required to match the LDT throughput is approximately 1080 °C assuming the more conservative depletion rate factor, which is about 30 °C higher than the measured temperatures noted above. The lower depletion rate factor would require a temperature closer to 1130 °C to match the observed depletion depths. About 10 mm upstream, the temperature drops to approximately 980 °C, and the expected depletion depth is then 15 – 30 μm at that axial location.

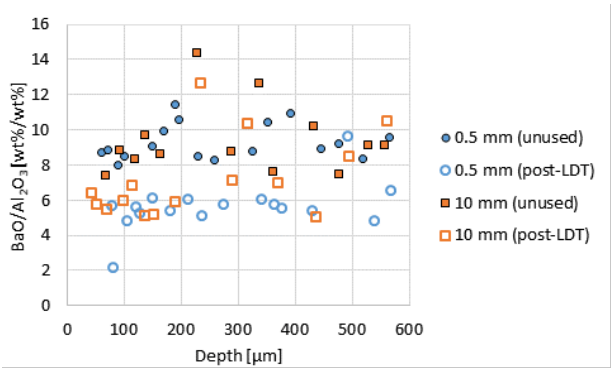

Figure 13: Estimated weight ratio of barium oxide to aluminum oxide in pores at various axial and radial locations for an unused and the post-LDT DCA insert

However, it should be noted that while depletion depths near the inner radius do not appear to be significant, the overall barium levels across the whole thickness and length of the post-LDT insert appear to be lower by about 30%

than compared to the unused insert in general.[55] A mechanism for barium loss deep within the insert is unknown, as examination of a cross section of the insert show that the pores are completely filled with the impregnate. Assuming it is not due to a manufacturing process deviation, perhaps it could be due to diffusion through the solid impregnate. However the profile of barium across the radial depth does not appear to match a typical diffusion gradient. Another possibility is that the diffusion rate through the solid impregnate is sufficiently high enough to maintain a relatively even distribution of barium across the radial depth and the rate limiting item is rather barium depletion at the active inner radius. If this depletion rate is assumed to be relatively constant over the LDT, then a reduction of 70%—that is, a barium content 30% of the original concentration, a crude bulk depletion limit—would require over 2100 kg of total throughput.

As mentioned above, apart from barium depletion, there are a few other processes that can lead to emitter degradation.[56] Tungstate formation will effectively lock barium and prevent it from contributing to a lower work function. Other various oxide or poisoning layers can also form that also effectively lock the barium from efficient emission. Examination of the used and unused DCA inserts using X-ray diffraction (XRD) techniques was performed to assess the crystal structure of the compounds on the inner surface of the insert.[55] A cobalt radiation parallel beam XRD diffractometer in a Bragg-Brentano configuration with a sample spot size ranging from 4 mm to 20 mm axial was used. The XRD results for the unused insert showed clean and single phase tungsten, as would be expected. For the post-LDT DCA insert, tungsten was still dominant, but dibarium calcium tungstate (Ba_2CaWO_6) was observed with a weight fraction of approximately 5%. No other tungstate forms were found. This translates to a molar fraction of less than 2% on the inner surface of the post-LDT DCA insert. Scanning electron microscope (SEM) images of both used and unused inserts show in Figure 14 how these tungstates are distributed on the surface.[55] For the used insert image on the right, the darker color regions are tungstates while the lighter regions are pure tungsten. The tungstates are seen to be a finer structure laying on top of the tungsten surface. The overall grain and pore sizes between the used and unused are similar in size, indicating that the surface morphology has not been altered significantly over the course of the LDT. There also does not appear to be any transported tungsten that are blocking or restricting pores and subsequently barium diffusion.

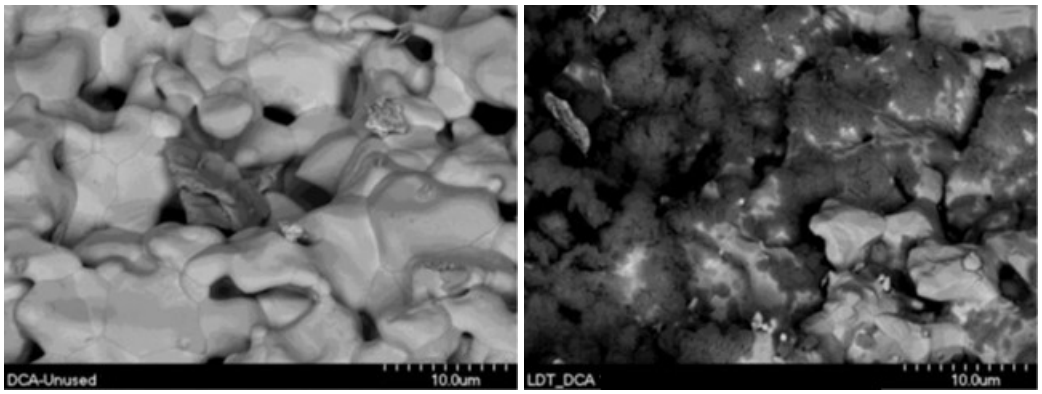

Figure 14: SEM images of the unused (left) and post-LDT (right) DCA insert inner surface

Overall, the post-LDT inspections of the DCA insert do not show any significant degradation. Tungstate formation is relatively minor and does not appear to be significantly locking or blocking barium transport. Free tungsten transport appears to be minimal and also not significantly affecting the insert pores. The observed barium depletion depths are contained to the downstream end of the insert and less than 100 μm of depletion was observed. The overall barium intensity relative to aluminum across the entire thickness of the insert did appear to decrease, as compared to the unused insert levels, but it is unclear if this is direct evidence of overall barium depletion. In addition to the post-test destructive analysis of the insert, the performance of the cathode over the duration of the LDT also provides confidence that even any emitter degradation that may not have been detected via the means above did not result in poor ignition or operation performance. At the conclusion of the LDT, the discharge cathode was ignited using only a slow ramping applied DC voltage rather than the nominal pulsing ignition sequence. The DCA was successfully ignited on both tries at voltages below 45 V with no indications of any severe cathode degradation. In summary, the overall life-limiting mechanism of the NEXT DCA emitter based on the LDT observations may be bulk barium depletion where 2100 kg of throughput is expected before reaching a soft failure criteria of a bulk depletion level of 30%.

C5. Heater failure

The life of the cathode heaters are primarily assessed through dedicated cyclic life testing. Only a few hundred cycles were placed on the cathode heaters during the LDT, which is insufficient to assess heater cyclic life. The post-LDT observations of the DCA heater found the coil to be in generally excellent condition. However, the LDT did experience intermittent, thermally-induced DCA heater open circuit occurrences during cathode conditioning and ignition. This was suspected to be due to poor contact between the heater sheath and cathode tube where a friction fit provided the current return path. Post-test inspection and resistance measurements revealed that the contact between the heater sheath and cathode tube was highly variable and indicated poor contact.[26] However, the NEXT PM design includes an improved return path through a metallized surface and braze material on the isolator that provides a reliable bonded contact and removes this particular issue via design.

Apart from the above issue, there still exists a gradual wear mechanism as the heaters undergo a large number of thermal cycles. Prior heater testing of the DCA heater geometry was performed as a pathfinder effort,[25] but a more recent test assessed the PM cathode heater design, materials, and fabrication procedures.[57] Three ½" DCA heaters were cyclically tested and accumulated 19059, 21626, and 33551 cycles before failure. Two-parameter Weibull analysis is performed to fit a shape, β, and scale, η, parameters for the cumulative failure distribution function,

$$F(t) = 1 - e^{-\left(\frac{t}{\eta}\right)^{\beta}} \tag{6}$$

Several methods are available to perform such an analysis such as rank regression evaluation or maximum likelihood estimates (MLE). Due to the small sample size and their relative spread, the resulting uncertainty and confidence levels of the fits are correspondingly wide. The Monte Carlo Markov chain calculation of the MLE approach confidence levels are shown on the left side of Figure 15. The median rank are shown in the circular data points with the 5% and 95% ranks illustrated as error bars on the right side of Figure 15. The wide spread of the data pushes the resulting 90% confidence B_{10} life—that is, the two-sided 90% confidence bound of the lifetime up to which 10% of the units fail—to relatively low values of 4000 to 5500 cycles as shown in Table 7 for different fit methods. This is primarily due to the last heater to fail (with 33551 cycles) that compared to the other DCA and even NCA heaters discussed later, appears to be somewhat of an outlier. If that heater had failed earlier, then the shape parameter would be higher and the distribution narrower, leading to an increased B_{10} life. As is, it should be clearly noted that the first failure was in excess of 19000 cycles which is well beyond prior cathode heater cycling life experienced with the International Space Station (ISS) Plasma Contactor Units (PCU), NSTAR, or NEXT cathodes.[25,58] The 90% confidence interval B_{10} life values shown in Table 7 are then a rather conservative lower bound on the expected cycle life for the DCA heaters. Other common cycle life criteria, such as demonstration of twice the mission cycle requirement, will generally result in much higher expected life.

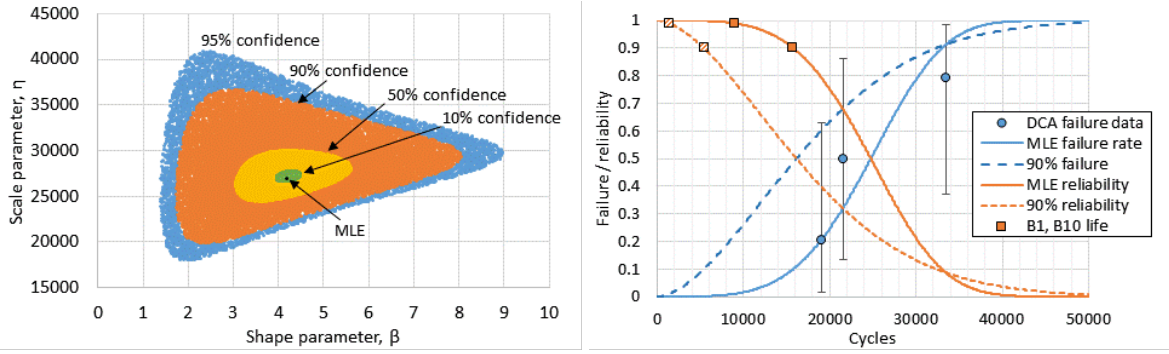

Figure 15: Maximum likelihood estimate (MLE) confidence level contours (left) and resultant failure and reliability curves (right) for the DCA heater

Table 7: Estimated DCA heater Weibull parameters and calculated B_{10} life

	Median rank / maximum likelihood			90% confidence interval		
Method	**Shape parameter, β**	**Scale parameter, η**	**B_{10} life**	**Shape parameter, β**	**Scale parameter, η**	**B_{10} life**
Y-rank regression	3.01	27958	13229	1.43	20055	4174
X-rank regression	3.52	27343	14430	1.68	20587	5387
Maximum likelihood	4.18	27022	15764	1.72	19935	5406

V. Neutralizer Cathode

D1. Keeper erosion

The neutralizer cathode has two main differences from the discharge cathode that affect its wear mechanisms: its operating conditions (and therefore also geometry) and its environment outside of the thruster discharge chamber. The lower operating current of the neutralizer cathode and its location exposed to facility backsputter result in primarily deposition rather than erosion on most of the keeper surfaces. Deposition was observed on nearly all surfaces of the keeper. In fact, the carbon buildup on the downstream face was found to be even thicker than would be expected by the measured facility backsputter rates during the LDT.[26]

The one exception to net deposition during the LDT was the outer diameter of the keeper tube facing the main ion beam of the thruster. At that location, for the LDT, a net erosion of up to nearly 25% of the initial keeper tube thickness was observed at the downstream edge.[26] Erosion of the keeper tube is primarily from the high energy beam ions striking the keeper surface.[59] The downstream tip of the cathode is approximately 75° from the thrust axis, and measurements of the NEXT beam current density profiles show a non-negligible population of beam ions at that angle.[8] The ion energy will be approximately equal to the applied beam voltage with corrections for ground and the neutralizer keeper voltages. The ratios of doubly and triply charged ions are included based on measurements near the edges of the accelerator grid.[8] These populations are relatively low, and again, since the sputter yield profile around the beam energies are relatively flat (i.e. not spanning orders of magnitude), doubling or tripling the ion impact energy is not enough to overcome their low flux ratios. Ultimately it was calculated that the doubles contribute 1 – 3% of the total erosion and the effect of the triples are nearly negligible.

The sputter yields of the keeper material were applied to calculate the expected erosion rates.[34] In addition to the energy dependent sputter yields at normal incidence, the angular contribution is also needed. The local ion incident angle for the side of the keeper facing the center of the thruster is assumed to be approximately 15° based on the location of the keeper tip. Based on the sparse angular sputter yield data available, the yield with a 15° incidence angle is approximately 10% higher than the yield at normal incidence, and this relative increase is used for the erosion calculations.

Applying the erosion calculations to the LDT throttling profile and durations produced a maximum erosion depth of approximately 125 μm near the downstream tip of the keeper. This is comparable to the maximum erosion depth of approximately 120 μm from the post-LDT analysis. In general, the highest erosion rate is observed for the TL40 throttle point. A soft failure criterion is the complete erosion through the thickness of the keeper tube, exposing the cathode and heater to the beam discharge. The neutralizer and thruster can still operate at this point, but will eventually face a hard failure when the neutralizer heater is subsequently eroded sufficiently to preclude cathode ignition. It should also be noted that the flight-like design implements a 50% thicker keeper tube thickness as compared to the engineering design operated in the LDT.[28] Using the soft failure criterion translates into a life of over 235 kh, or an equivalent throughput of over 4800 kg of xenon at TL40 before the downstream edge of the keeper is eroded away and the tip of the cathode is exposed.

D2. Cathode orifice plate erosion

While only net deposition was observed for the neutralizer keeper orifice during the LDT, net erosion was observed on portions of the cathode orifice plate, particularly in the chamfer region.[26] The erosion of the neutralizer orifice plate is suspected to have led to a drop in the keeper voltage and loss of flow margin over the first 19.5 kh (~400 kg throughput) of operation.[3,60,61] This is corroborated by a model of the NEXT NCA which show that enlargement of

the orifice will lead to a drop in the keeper voltage.[62] Some additional loss of both parameters were observed with the final portion of high power operation, but largely negligible after 650 kg of total throughput.[3] In addition—through in-situ visual observation and measurement—the orifice chamfer diameter was observed to increase by 20% over the first 15 kh (~300 kg throughput) or so and relatively stable thereafter.[3] These indications appear to show that the erosion was greatest during the initial portion of LDT testing at high power, but largely tapered off after 300 – 400 kg of throughput and became negligible after 650 kg of total throughput (580 kg throughput at high beam current).

The primary failure mechanism arising from NCA orifice erosion is the loss of flow margin and the cathode transitioning to an oscillatory plume mode which will exacerbate erosion and eventual failure of the cathode to operate. The loss in flow margin has been since mitigated by relatively minor changes in the cathode design and the nominal neutralizer flow rates so as to provide a sufficient margin over the worst case and preclude the neutralizer from entering plume mode. The flow margin at worst case, even without the design change, was estimated to be a minimum of 0.4 sccm, which is already greater than the flow margin at beginning of life with the prior throttle table at low beam currents.[3] The design changes only provide further margin before transition to plume mode operation. In addition, a plume mode detection circuit is implemented in the NEXT PPU.[63] This provides another layer of protection by allowing the operator to increase the flow rate to return the neutralizer to spot mode operation if plume mode onset is detected.

D3. Orifice clogging

Similar to the discharge cathode, net deposition was observed on the upstream end of the barrel section of the neutralizer cathode orifice.[26] However, the quantity of deposition observed during and after the LDT was relatively minor, with the minimum orifice diameter found to be around 8% smaller by the end of the LDT. In addition, this deposition was also found to be of the same material as the orifice plate, likely originating from the downstream portions of the orifice plate which did erode. As stated above, it is suspected that the downstream portions of the orifice plate primarily eroded during the first 19.5 kh of high power operation of the LDT. In contrast, neutralizer orifice clogging was observed primarily during low power operation for the NSTAR ELT. The DC and AC characteristics of the neutralizer-keeper voltage and current were seen to increase after 0.8 kh of low power operation and in situ visual inspection after 5.7 kh revealed the orifice was over 50% blocked.[54] For the NEXT LDT, the thruster was operated for 9.7 kh at low power operation. The DC and AC characteristics did not exhibit indications of clogging. Nor did in-situ visual diameter measurements show any evidence of clogging during low power operation or even over the whole LDT duration.[3,61] This indicates changes in the NCA design and operation for NEXT—including nearly twice the orifice diameter, higher emission currents, and ensuring sufficient keeper current—have largely removed cathode orifice deposition and clogging as a potential failure mode.

D4. Barium insert degradation

Barium depletion or other mechanisms limiting the ability of the barium impregnate to maintain a sufficiently low work function can also be a failure mode for the neutralizer cathode. The same analysis method can be applied to the neutralizer cathode insert as was performed for the discharge cathode above. The NEXT neutralizer cathode operates with a fixed keeper current of 3 A. With a maximum thruster operating beam current of 3.52 A, the maximum emission current for the NEXT neutralizer cathode is then 6.52 A. A peak insert temperature of 1050 °C is estimated from insert temperature measurements of a cathode with the same emitter and orifice geometry as the NEXT neutralizer cathode.[51] This is similar to the peak measured DCA insert temperatures and based on the trends shown above in Figure 12, it is expected that insert barium will not reach depletion for at least a throughput of 2750 kg at the worst case emission current. Again, this analysis approach is very conservative in its assumptions as the temperatures drop 50 °C over a few mm further upstream in addition to the barium recycling expected in the hollow cathode geometry that greatly extends barium availability.

Similar to the DCA analysis, the post-test destructive examination of the NCA insert did not show barium depletion on the level of the above simplistic model.[55] In fact, the EDS measurements of the barium to aluminum concentrations did not exhibit any conclusive signs of a depletion depth at all as seen in Figure 16. While the DCA insert analysis estimated about a 30% drop in overall barium ratios compared to the unused insert, here for the NCA, no significant decrease exceeding the measurement uncertainty is noted. This would suggest that minimal barium was lost from the cathode and that it was effectively recycled or otherwise retained over the course of the LDT.

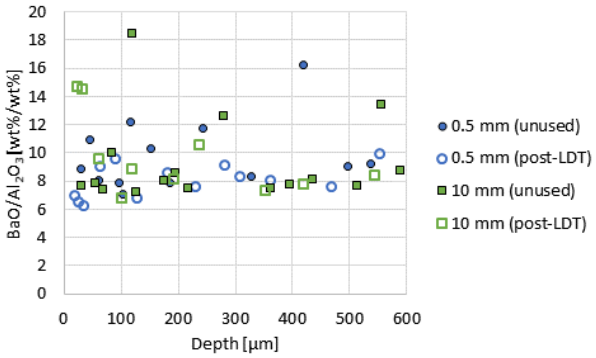

Figure 16: Estimated weight ratio of barium oxide to aluminum oxide in pores at various axial and radial locations for an unused and the post-LDT NCA insert

The NCA insert was also examined via XRD analysis to investigate the presence and composition of various tungstates on the inner surface.[55] Here, the results were much more variegated than as was observed with the DCA which was fairly uniform along the axial position and with only a single tungstate compound detected. The first observation is that distinct banded regions are observed along the axial direction of the NCA. A banded appearance was also noted in other cathode inserts: after the 8200 h NSTAR LDT and after the 45 kh life test of a JAXA cathode.[29,64] These regions were found to have drastically different compositions for the NEXT NCA insert as identified via XRD interrogation. Beginning with the upstream end, four barium tungstates were detected, Ba_3WO_6, Ba_2WO_5, $BaWO_4$, $Ba_3W_2O_9$. These correspond to the stoichiometric 3:1, 2:1, 1:1, and 3:2 ratios of the BaO and WO_3 oxides. Two of the tungstates, Ba_3WO_6 and $BaWO_4$, are expected as reaction products resulting from the reduction of BaO on tungsten and the subsequent thermal decomposition.[65] Ba_2WO_5 and $Ba_3W_2O_9$ are the intermediate compounds that are thermally stable between 800 – 1000 °C,[66,67] which well envelops the expected temperature at this axial location based on measurements of a similar cathode and insert.[51]

The middle section of the NCA insert was observed to consist of primarily barium aluminates $Ba_4Al_2O_7$ and $Ba_3Al_2O_6$ as well as some barium tungstate Ba_3WO_6. The two aluminates identified correspond to the 4:1 and 3:1 ratios of the BaO and Al_2O_3 oxides and the stable phases above 940 °C.[68] These two aluminates are suspected to play an important role in the release of barium oxide, although other aluminate compounds were not observed on the surface of the NCA insert.[69]

The light colored region near the downstream end is found to consist primarily of alstonite, $BaCa(CO_3)_2$. Alstonite is a double salt consisting of the two carbonates $BaCO_3$ and $CaCO_3$, which are also two of the compounds used in the synthesis of the impregnate. However, during impregnate formation, temperatures in the 1100-1200 °C range are needed to drive off the carbon as carbon dioxide and form the oxides.[70] Since the NCA operational insert temperatures are typically well below this range, the carbon is perhaps more likely to remain locked into the surface compounds. The carbon likely originated from facility backsputter, then entered the cathode and reacted with the barium and calcium oxides on the insert surface. As noted earlier, the carbon deposition on the downstream face of the NCA keeper was substantial. In addition, the visible downstream demarcation of the visible alstonite phase is aligned with the expected shadow shielding provided by the orifice geometry further supporting the theory that the carbon originated from the facility and is an artifact of ground facility testing.

Despite the presence of these various compounds on the active surface of the NCA insert, no performance degradation was noted over the course of the LDT. Some of the compounds, including the upstream tungstates and the mid-region aluminates, are known to be active in free barium and barium oxide production, so it would be expected that these regions are active zones. While the impact of alstonite on the overall work function and potential binding of barium is unclear, this is a ground facility effect and would not be observed in a flight environment. Without any carbon present, it is speculated that this region would form Ba_2CaWO_6 tungstate similar to the DCA and other cathodes. The Ba_2CaWO_6 tungstate form is a known effective electron emitter, so it wouldn't necessarily signal end of life if the emitter is carpeted with this tungstate.

SEM images of the NCA insert inner surface show that there are noticeable morphology changes at various locations on the used cathode as shown in Figure 17.[55] This is in contrast to the DCA, where minor differences were observed. While the various compounds described above may form these different surface structures, the surface layers are still observed to be porous and do not completely block or prohibit barium transport. Also, as mentioned above, many of the compounds observed on the surface are either involved in the free barium reactions or are relatively

decent electron emitters themselves. Again, the NCA cathode did not observe any impact to its performance or ignition characteristics over the duration of the LDT that would be due to emitter degradation. It is expected that the NCA could operate for a substantially longer duration beyond the LDT demonstration. The conservative theoretical analysis predicts well beyond 2750 kg of throughput, and the post-LDT analysis of the NCA insert did not uncover any other more limiting mechanisms.

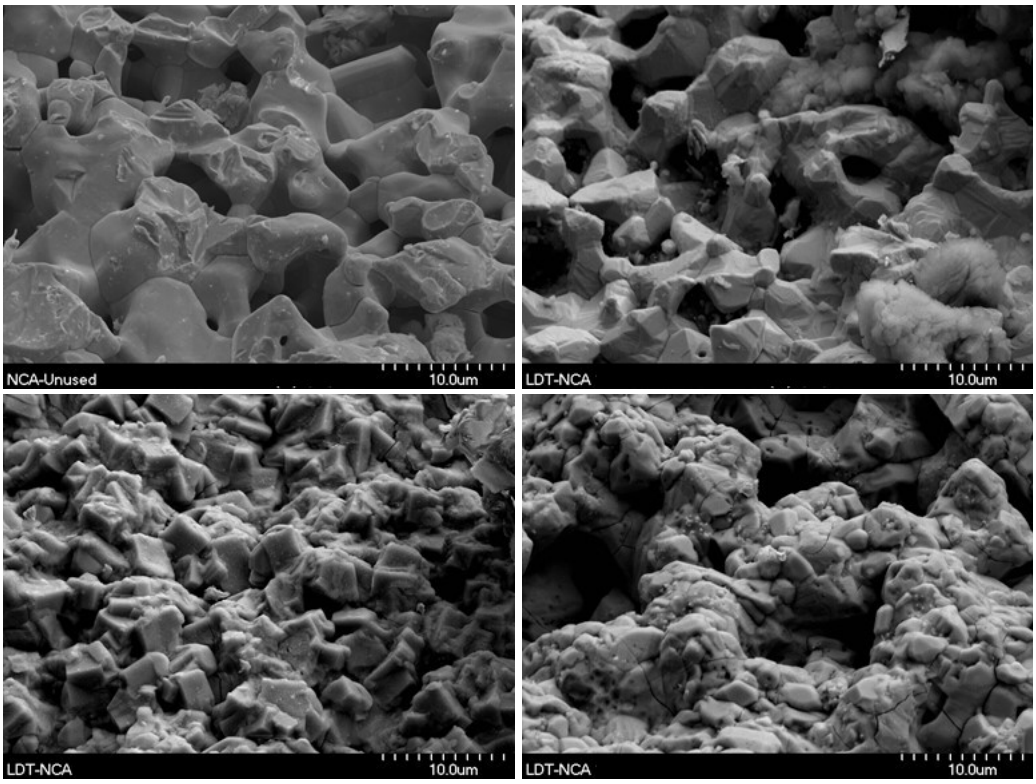

Figure 17: SEM images of the unused (top-left) and post-LDT downstream (top-right), middle (bottom-right), and upstream (bottom-left) NCA insert inner surface

D5. Heater failure

The post-LDT observations of the NCA heater found the coil to be in excellent condition. No return path open circuits issues were detected, and no impacts to NCA ignition due to any other aspects of heater operation were noted. The same cyclic life testing was performed for the NCA heater as was done for the DCA as described above.[57] Three ¼" NCA heaters were tested to failure and they accumulated cycle counts of 21479, 25117, and 27700. The same set of Weibull analyses were performed and the results are presented below in Figure 18 and Table 8. Note that only the two-sided 90% (or equivalently one-sided 95%) confidence interval results are shown in Table 8 for brevity. Here for the NCA heaters, in contrast with the DCA results, the 90% confidence parameters are much closer to the median and MLE values due to the tighter grouping of failure data. Even a 2x cycle life demonstration provides over 10000 expected cycles for the NCA heaters.

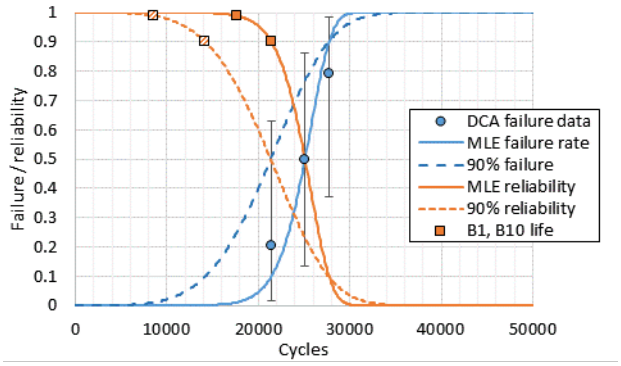

Figure 18: NCA heater failure rate and reliability

Table 8: Estimated NCA heater Weibull parameters and calculated B_{10} life

		90% confidence interval	
Method	**Shape parameter, β**	**Scale parameter, η**	**B_{10} life**
Y-rank regression	3.58	22923	12236
X-rank regression	3.59	22927	12257
Maximum likelihood	4.62	23109	14204

VI. Summary and conclusion

A summary of the NEXT failure modes and status of the service life assessment for each are presented below in Table 9. As described in the beginning of this report, these failure modes were each assessed to fall into one of three categories (gradual wear, probabilistic event, and eliminated via design) and addressed accordingly. Apart from accelerator grid erosion, the next most restrictive life limiting mechanism may be barium depletion of the DCA inserts as evidenced by the measured decrease of bulk barium levels for the post-LDT inserts as compared to unused inserts. It was noted in the section above that this is much different from prior insert barium depletion analysis, where a depletion depth is the main mechanism and not a bulk decrease. It is not conclusive that this is a real phenomenon or if it is an artifact of an outlier insert. Even so, more than 2100 kg of propellant throughput can be expected to be achieved with NEXT before the barium levels drop too low to be an effective electron source.

A few other mechanisms will lead to certain potential failure events; these include intermittent grid shorting from debris, DCA cathode-keeper shorting, and tungstate formation on the cathode insert surfaces. However, as discussed more extensively above, the first two are addressed via established mitigation methods and the latter has not shown any effects in performance or operation degradation. Indeed these and all other potential failure modes, known and even any unknown, were not demonstrated to cause a failure of the NEXT thruster over the 50 kh and 900 kg of the LDT. It is expected from the post-test analysis documented in this report that many of these failure modes will not occur for a substantially longer duration than demonstrated by the LDT. Of course, the analysis of the accelerator grid erosion mechanisms still needs to be completed to provide the whole picture and overall service life expectation for NEXT.

Table 9: Assessment of NEXT failure modes

	Failure mechanism	Status
A1	Pit and groove erosion of accelerator grid	Prior estimate of 330 kg or 36 kh based on throttle point[2]
A2	Accelerator grid aperture enlargement	Prior estimate of only 10 V impact on backstreaming margin[2]
A3	Accelerator grid rogue hole formation	Extremely conservative analysis of rogue hole generation predicts ≫ 2650 kg of throughput before soft failure
A4	Screen grid erosion	Conservative analysis at worst-case conditions still predicts > 4100 kg of throughput before potential failure
A5	Contamination debris grid shorting	Mitigated by flight environment and process controls to reduce flake generation and foreign debris; recycles, thermal soaks, and grid clearing circuit available to clear instances of low impedance
B1	Degradation of magnetic field strength	Temperatures well below concern; not an expected failure mode
B2	Degradation of electrical isolation	Proper design of propellant isolators, plasma screens, and shadow shielding remove mechanisms of impedance loss
C1	Erosion of discharge cathode keeper	Assuming worst case erosion requires > 3500 kg of throughput to erode through thickness of DCA keeper orifice plate to expose heater
C2	Erosion of discharge cathode orifice	Assuming worst case erosion requires > 3400 kg of throughput to erode through thickness of DCA cathode orifice plate
C3	Deposition leading to DCA keeper-cathode short	DCA keeper-cathode short may be expected after 265 kg throughput at high current operation, but does not lead to direct failure; potential impacts are addressed by mitigation procedures for extinguish restart and longer cathode ignitions
C4	Degradation of DCA insert	Conservative analysis of bulk barium depletion predicts > 2100 kg of throughput before soft failure
C5	Degradation of DCA heater insulation or conductor	Heater-cathode gap open circuit failure eliminated via design; Conservative Weibull analysis of cycle life test data predicts > 4100 cycles before heater failure
D1	Erosion of neutralizer cathode keeper	Conservative analysis at worst-case conditions still predicts > 4800 kg of throughput before soft failure
D2	Erosion of neutralizer cathode orifice	Indications of erosion negligible after reaching steady-state profile; geometry and throttle table changes as well as PPU detection circuit further prevent soft failure of plume mode onset
D3	Deposition leading to NCA orifice clogging	Not observed over 9.7 kh of low power operation, indicating it is likely removed as a potential failure mode via design
D4	Degradation of NCA insert	Extremely conservative analysis at worst-case conditions still predicts ≫ 2750 kg of throughput before soft failure from barium depletion
D5	Degradation of NCA heater insulation or conductor	Conservative Weibull analysis of cycle life test data predicts > 12200 cycles before heater failure

Acknowledgments

The authors would like to acknowledge the other past and present members of the NEXT team and the extensive work that has been performed over the course of the past decade to test, analyze, and characterize NEXT and its components that has provided much of the source data for this life assessment. This work was funded by the NEXT-C project, which is led by NASA GRC under NASA's Science Mission Directorate.

References

[1]Van Noord, J. L., "Lifetime assessment of the NEXT ion thruster," *43rd AIAA/ASME/SAE/ASEE Joint Propulsion Conference and Exhibit*, AIAA-2007-5247, 2007.

[2]Van Noord, J. L., and Herman, D. A., "Application of the NEXT ion thruster lifetime assessment to thruster throttling," *44th AIAA/ASME/SAE/ASEE Joint Propulsion Conference and Exhibit*, AIAA-2008-4526, 2008.

[3]Shastry, R., Herman, D. A., Soulas, G. C., and Patterson, M. J., "End-of-test performance and wear characterization of NASA's evolutionary xenon thruster (NEXT) long-duration test," *50th AIAA/ASME/SAE/ASEE Joint Propulsion Conference and Exhibit*, AIAA-2014-3617, 2014.

[4]Brophy, J. R., Polk, J. E., Randolph, T. M., and Dankanich, J. W., "Lifetime qualification of electric thrusters for deep-space missions," *44th AIAA/ASME/SAE/ASEE Joint Propulsion Conference and Exhibit*, AIAA-2008-5184, 2008.

[5]Goebel, D. M., Polk, J. E., Wirz, R. E., Snyder, J. S., Mikellides, I. G., Katz, I., Anderson, J., "Qualification of commercial XIPS ion thrusters for NASA deep space missions," *44th AIAA/ASME/SAE/ASEE Joint Propulsion Conference and Exhibit*, AIAA-2008-4914, 2008.

[6]Soulas, G. C., and Shastry, R., "Post-test inspection of NASA's evolutionary xenon thruster long duration test hardware: ion optics," *52nd AIAA/ASME/SAE/ASEE Joint Propulsion Conference and Exhibit*, AIAA-2016-4632, 2016.

[7]Soulas, G. C., "The impact of back-sputtered carbon on the accelerator grid wear rates of the NEXT and NSTAR ion thrusters," *33rd International Electric Propulsion Conference*, IEPC-2013-157, 2013.

[8]Pollard, J. E., Diamant, K. D., Crofton, M. W., Patterson, M. J., and Soulas, G. C., "Spatially-resolved beam current and charge-state distributions for the NEXT ion engine," *46th AIAA/ASME/SAE/ASEE Joint Propulsion Conference and Exhibit*, AIAA-2006-6779, 2006.

[9]Herman, D. A., and Gallimore, A. D., "Discharge chamber plasma potential mapping of a 40-cm NEXT-type ion engine," *41st AIAA/ASME/SAE/ASEE Joint Propulsion Conference and Exhibit*, AIAA-2005-4251, 2005.

[10]Doerner, R. P., Whyte, D. G., and Goebel, D. M., "Sputtering yield measurements during low energy xenon plasma bombardment," *Journal of Applied Physics*, v. 93, n. 9, pp. 5816-5823, 2003.

[11]Young, W. C., *Roark's Formulas for Stress & Strain*, McGraw-Hill, Inc., 1989.

[12]O'Donnell, W. J., "Effective elastic constants for the bending of thin perforated plates with triangular and square penetration patterns," *Journal of Engineering for Industry*, v. 95, i. 1, pp. 121-128, 1973.

[13]O'Donnell, W. J., and Langer, B. F., "Design of perforated plates," *Journal of Engineering for Industry*, v. 84, i. 3, pp. 307-319, 1962.

[14]Shastry, R., and Soulas, G. C., "Post-test inspection of NASA's evolutionary xenon thruster long duration test hardware: discharge chamber," *52nd AIAA/ASME/SAE/ASEE Joint Propulsion Conference and Exhibit*, AIAA-2016-4630, 2016.

[15]de Groh, K. K., Banks, B. A., and Karniotis, C. A., "NSTAR extended life test discharge chamber flake analyses," *40th AIAA/ASME/SAE/ASEE Joint Propulsion Conference and Exhibit*, AIAA-2004-3612, 2004.

[16]Garner, C. E., and Rayman, M. D., "In-flight operation of the Dawn ion propulsion system through completion of Dawn's primary mission," *52nd AIAA/ASME/SAE/ASEE Joint Propulsion Conference and Exhibit*, AIAA-2016-4539, 2016.

[17]Soulas, G. C., "Calculation of thermally-induced displacements in spherically domed ion engine grids," *29th International Electric Propulsion Conference*, IEPC-2005-248, 2005.

[18]Anderson, J. R., Vaughn, D., and Fitzgerald, D., "Experimental and theoretical analysis for designing a grid clearing system for the NEXT ion propulsion system," *41st AIAA/ASME/SAE/ASEE Joint Propulsion Conference and Exhibit*, AIAA–2005–3866, 2005.

[19]Piñero, L. R., Hopson, M., Todd, P. C., and Wong, B., "Performance of the NEXT engineering model power processing unit," *43rd AIAA/ASME/SAE/ASEE Joint Propulsion Conference and Exhibit*, AIAA-2007-5214, 2007.

[20]Soulas, G. C., Domonkos, M. T., and Patterson, M. J., "Performance evaluation of the NEXT ion engine," *39th AIAA/ASME/SAE/ASEE Joint Propulsion Conference and Exhibit*, AIAA-2003-5278, 2003.

[21]Anderson, J. R., Snyder, J. S., Van Noord, J. L., and Soulas, G. C., "Thermal development test of the NEXT PM1 ion engine," *43rd AIAA/ASME/SAE/ASEE Joint Propulsion Conference and Exhibit*, AIAA-2007-5217, 2007.

[22]Liu, J., Vora, P., Dent, P., Walmer, M., Chen, C., Talnagi, J., Wu, S., and Harmer, M., "Thermal stability and radiation resistance of Sm-Co based permanent magnets," *Space Nuclear Conference 2007*, 2036, 2007.

[23]Mantenieks, M. A., "Investigation of mercury thruster isolators," *AIAA 10th Electric Propulsion Conference*, AIAA-1973-1088, 1973.

[24]Mantenieks, M. A., "Status of 30-centimeter-diameter mercury ion thruster isolator development," *AIAA 12th Electric Propulsion Conference*, AIAA-1976-1027, 1976.

[25]Herman, D. A., Pinero, L., R., and Sovey, J. S., "NASA's evolutionary xenon thruster (NEXT) component verification testing," *44th AIAA/ASME/SAE/ASEE Joint Propulsion Conference and Exhibit*, AIAA-2008-4812, 2008.

[26]Shastry, R., and Soulas, G. C., "Post-test inspection of NASA's evolutionary xenon thruster long-duration test hardware: discharge and neutralizer cathodes," *52nd AIAA/ASME/SAE/ASEE Joint Propulsion Conference & Exhibit*, AIAA-2016-4631, 2016.

[27]Domonkos, M. T., Foster, J. E., Soulas, G. C., and Nakles, M., "Testing and analysis of NEXT ion engine discharge cathode assembly wear," *39th AIAA/ASME/SAE/ASEE Joint Propulsion Conference and Exhibit*, AIAA-2003-4864, 2003.

[28]Soulas, G. C., Kamhawi, H., Patterson, M. J., Britton, M. A., and Frandina, M. M., "NEXT ion engine 2000 hour wear test results," *40th AIAA/ASME/SAE/ASEE Joint Propulsion Conference and Exhibit*, AIAA-2004-3791, 2004.

[29]Polk, J. E., Anderson, J. R., Brophy, J. R., Rawlin, V. K., Patterson, M. J., Sovey, J., and Hamley, J., "An overview of the results from the 8300 hour wear test of the NSTAR ion thruster," *35th AIAA/ASME/SAE/ASEE Joint Propulsion Conference and Exhibit*, AIAA-1999-2446, 1999.

[30]Kolasinski, R. D., Polk, J. E., Goebel, D., and Johnson, L. K., "Carbon sputtering yield measurements at grazing incidence," *Applied Surface Science*, v. 254, pp. 2506-2515, 2008.

[31]Tartz, M., Neumann, H., Leiter, H., and Esch, J., "Pyrolytic graphite and carbon-carbon sputter behavior under xenon ion incidence," *29th International Electric Propulsion Conference*, IEPC-2005-143, 2005.

[32]Williams, J. D., Johnson, M. L., and Williams, D. D., "Differential sputtering behavior of pyrolytic graphite and carbon-carbon composite under xenon bombardment," *40th AIAA/ASME/SAE/ASEE Joint Propulsion Conference & Exhibit*, AIAA-2004-3788, 2004.

[33]Deltschew, R., et al.., "Sputter characteristics of carbon-carbon compound material," *27th International Electric Propulsion Conference*, Pasadena, CA, IEPC-01-118, 2001.

[34]Yim, J. T., "A survey of xenon ion sputter yield data and fits relevant to electric propulsion spacecraft integration," *35th International Electric Propulsion Conference*, IEPC-2017-060, 2017.

[35]Wei, Q., Li, K.-D., Lian, J., and Wang, L., "Angular dependence of sputtering yield of amorphous and polycrystalline materials," *Journal of Physics D: Applied Physics*, v. 41, 172002, 2008.

[36]Sengupta, A., Brophy, J. R., Anderson, J. R., Garner, C., de Groh, K., Karniotis, T., and Banks, B., "An overview of the results from the 30,000 h life test of deep space 1 flight spare ion engine," *40th AIAA/ASME/SAE/ASEE Joint Propulsion Conference & Exhibit*, AIAA-2004-3608, 2004.

[37]Fife, J., Gibbons, M., Hargus, Jr., W., VanGilder, D., Kirtley, D., and Johnson, L., "3-D computation of surface sputtering and redeposition due to hall thruster plumes," *28th International Electric Propulsion Conference*, Toulouse, IEPC-2003-0136, 2003.

[38]Yamamura, Y., and Tawara, H., "Energy dependence of ion-induced sputtering yields from monatomic solids at normal incidence," *Atomic Data and Nuclear Data Tables*, v. 62, pp. 149-253, 1996.

[39]Yamamura, Y., "An empirical formula for angular dependence of sputtering yields," *Radiation Effects*, v. 80, pp. 57-72, 1984.

[40]Yamamura, Y., "Contribution of anisotropic velocity distribution of recoil atoms to sputtering yields and angular distributions of sputtered atoms," *Radiation Effects*, v. 55, pp. 49-56, 1981.

[41]Mikellides, I. G. and Katz, I., "Wear mechanisms in electron sources for ion propulsion, 1: neutralizer hollow cathode," *Journal of Propulsion and Power*, v. 24, n. 4, pp. 855-865, 2008.

[42]Britton, M., Soulas, G., Kamhawi, H., and Snyder, A. "Destructive analysis of the NEXT 2000-hour wear test hollow cathode assemblies," NASA/TM—2005-213387, 2005.

[43]Kovaleski, S. D., "Life model of hollow cathodes using a barium calcium aluminate impregnated tungsten emitter," *27th International Electric Propulsion Conference*, IEPC-2001-276, 2001.

[44]Longo, R. T., "Physics of thermionic dispenser cathode aging," *Journal of Applied Physics*, v. 94, n. 10, pp. 6966-6975, 2003.

[45]Polk, J. E., Mikellides, I. G., Katz, I., and Capece, A. M., "Tungsten and barium transport in the internal plasma of hollow cathodes," *Journal of Applied Physics*, v. 105, 113301, 2009.

[46]Polk, J. E., Mikellides, I. G., Capece, A. M., and Katz, I., "Barium depletion in hollow cathode emitters," *Journal of Applied Physics*, v. 119, 023303, 2016.

[47]Rudwan, I. M. A., Wallace, N. C., Coletti, M., and Gabriel, S. B., "Emitter depletion measurement and modeling in the T5 & T6 Kaufman-type ion thrusters," *30th International Electric Propulsion Conference*, IEPC-2007-256, 2007.

[48]Paullel, P. and Shroff, A. M., "Experimental study of impregnated-cathode behavior, emission, and life," *Journal of Applied Physics*, v. 51, n. 5, pp. 2894-2902, 1980.

[49]Roquias, J. M., Poret, F., le Doze, R., Ricaud, J. L., Monterrin, A., and Steinbrunn, A., "Barium depletion study on impregnated cathodes and lifetime prediction," *Applied Surface Science*, v. 215, i. 1-4, pp. 5-17, 2003.

[50]Goebel, D. M., Katz, I., Polk, J., Mikellides, I. G., Jameson, K. K., Liu, T., and Dougherty, R., "Extending hollow cathode life for electric propulsion in long-term missions," *Space 2004 Conference and Exhibit*, AIAA-2004-5911, 2004.

[51]Polk, J., Marrese, C., Thornber, B., Dang, L., and Johnson, L., "Temperature distributions in hollow cathode emitters," *40th AIAA/ASME/SAE/ASEE Joint Propulsion Conference and Exhibit*, AIAA-2004-4116, 2004.

[52]Polk, J. E., Goebel, D. M., Watkins, R., Jameson, K., Yoneshige, L., Przybylowski, J., and Chu, L., "Characterization of hollow cathode performance and thermal behavior," *42nd AIAA/ASME/SAE/ASEE Joint Propulsion Conference and Exhibit*, AIAA-2006-5150, 2006.

[53]Soulas, G. C., and Patterson, M. J., "NEXT ion thruster performance dispersion analyses," *43rd AIAA/ASME/SAE/ASEE Joint Propulsion Conference and Exhibit*, AIAA-2007-5213, 2007.

[54]Sengupta, A., "Destructive physical analysis of hollow cathodes from the Deep Space 1 flight spare ion engine 30,000 h life test," *29th International Electric Propulsion Conference*, IEPC-2005-026, 2005.

[55]Mackey, J. A., Shastry, R., and Soulas, G. S., "Characterization of the NEXT hollow cathode inserts after long-duration testing," *35th International Electric Propulsion Conference*, IEPC-2017-304, 2017.

[56]Sarver-Verhey, T. R., "Scenario for hollow cathode end-of-life," NASA/CR—2000-209420, 2000.

[57]Sarver-Verhey, T. R., Soulas, G. S., and Mackey, J. A., "Heater validation for the NEXT-C hollow cathodes," *35th International Electric Propulsion Conference*, IEPC-2017-397, 2017.

[58]Patterson, M. J., Verhey, T. R., Soulas, G. S., and Zakany, J., "Space station cathode design, performance, and operating specifications," *25th International Electric Propulsion Conference*, IEPC-1997-170, 1997.

[59]Kuharski, R. A., Mandell, M. J., Gardner, B. M., Katz, I., and Vaughan, D., "Ion engine neutralizer erosion in lab and space," *41st AIAA/ASME/SAE/ASEE Joint Propulsion Conference and Exhibit*, AIAA-2005-3880, 2005.

[60]Herman, D. A., Soulas, G. C., and Patterson, M. J., "NEXT long-duration test neutralizer performance and erosion characteristics," *31st International Electric Propulsion Conference*, IEPC-2009-154, 2009.

[61]Herman, D. A., Soulas, G. C., Van Noord, J. L., and Patterson, M. J., "NASA's evolutionary xenon thruster long-duration test results," *Journal of Propulsion and Power*, v. 28, n. 3, pp. 625-635, 2012.

[62]Mikellides, I. G., Snyder, J. S., Goebel, D. M., Katz, I., and Herman, D. A., "Neutralizer hollow cathode simulations and comparison with ground test data," *31st International Electric Propulsion Conference*, IEPC-2009-20, 2009.

[63]Aulisio, M. V., Piñero, L. R., White, B. L., Hickman, T. A., Bontempo, J. J., Hertel, T. A., and Birchenough, A. G., "Status of the development of flight power processing units for the NASA's evolutionary xenon thruster – commercial (NEXT-C) project," *14th International Energy Conversion Engineering Conference*, AIAA-2016-4519, 2016.

[64]Ohkawa, Y., Higuchi, T., Hayakawa, Y., Miyazaki, K., and Nagano, H., "Observation and analysis of graphite hollow cathode after 45,000-hour life test," *33rd International Electric Propulsion Conference*, IEPC-2013-364, 2013

[65]Lipeles, R. A., and Kan, H. K. A., "Chemical stability of barium calcium aluminate dispenser cathode impregnants," *Applications of Surface Science*, v. 16, pp. 189-206, 1983.

[66]Kreidler, E. R., "Phase equilibria in the system CaO-BaO-WO3," *Journal of the American Chemical Society*, v. 55, n. 10, pp. 514-519, 1972.

[67]Poeppelmeier, K. R., Jacobson, A. J., and Longo, J. M., "The structure of Ba3W2O9; an example of face-shared octahedral with tungsten (VI)," *Materials Research Bulletin*, v. 15, i. 3, pp. 339-345, 1979.

[68]Wolten, G. M., "An appraisal of the ternary system BaO-CaO-Al2O3," SD-TR-80-67, TR-0080(5911)-1, 1980.

[69]Coletti, M. C., and Gabriel, S. B., "A model for barium oxide depletion from hollow cathode inserts," *IEEE Transactions on Plasma Science*, v. 37, n. 1, pp. 58-66, 2009.

[70]Cronin, J. L., "Modern dispenser cathodes," *IEE Proceedings I – Solid-State and Electron Devices*, v. 128, n. 1, pp. 19-32, 1981.